Thermoelastodynamic Responses of Panels Through Nonlinear Reduced Order

Modeling: Oscillating Flux and Temperature Dependent Properties

by

Andrew Matney

A Thesis Presented in Partial Fulfillment
of the Requirements for the Degree
Master of Science

Approved July 2011 by the
Graduate Supervisory Committee:

Marc Mignolet, Chair
Hanqing Jiang
Stephen Spottswood

ARIZONA STATE UNIVERSITY

August 2011

ABSTRACT

This thesis focuses on the continued extension, validation, and application of combined thermal-structural reduced order models for nonlinear geometric problems. The first part of the thesis focuses on the determination of the temperature distribution and structural response induced by an oscillating flux on the top surface of a flat panel. This flux is introduced here as a simplified representation of the thermal effects of an oscillating shock on a panel of a supersonic/hypersonic vehicle. Accordingly, a random acoustic excitation is also considered to act on the panel and the level of the thermo-acoustic excitation is assumed to be large enough to induce a nonlinear geometric response of the panel. Both temperature distribution and structural response are determined using recently proposed reduced order models and a complete one way, thermal-structural, coupling is enforced. A steady-state analysis of the thermal problem is first carried out that is then utilized in the structural reduced order model governing equations with and without the acoustic excitation. A detailed validation of the reduced order models is carried out by comparison with a few full finite element (Nastran) computations. The computational expedience of the reduced order models allows a detailed parametric study of the response as a function of the frequency of the oscillating flux. The nature of the corresponding structural ROM equations is seen to be of a Mathieu-type with Duffing nonlinearity (originating from the nonlinear geometric effects) with external harmonic excitation (associated with the thermal moments terms on the panel). A dominant resonance is observed and explained.

i

The second part of the thesis is focused on extending the formulation of the combined thermal-structural reduced order modeling method to include temperature dependent structural properties, more specifically of the elasticity tensor and the coefficient of thermal expansion. These properties were assumed to vary linearly with local temperature and it was found that the linear stiffness coefficients and the "thermal moment" terms then are cubic functions of the temperature generalized coordinates while the quadratic and cubic stiffness coefficients were only linear functions of these coordinates. A first validation of this reduced order modeling strategy was successfully carried out.

To my parents, for always believing in and supporting me.

ACKNOWLEDGEMENTS

TABLE OF CONTENTS

CHAPTER   Page

LIST OF FIGURES

LIST OF TABLES

CHAPTER 1 - INTRODUCTION

Notwithstanding the significant body of research existing in the literature,
the accurate, computationally efficient prediction of the dynamic response of
hypersonic aircraft panels remains an important and challenging problem. Its
complexity stems from (1) the severity of the loading (acoustic, thermal,
aerodynamic) that induces large, geometrically nonlinear motions of the structure,
and (2) the multi-disciplinary, structural - thermal - aerodynamic, coupling
present.

In recent years, the adoption of reduced order models for the prediction of
the structural response [1-13] has emerged as the option of choice to avoid the
computational burden associated with full finite element computations while
maintaining accuracy. In addition to this notable advantage, reduced order models
have also been found to be much more straightforward to couple with each other
than the corresponding full order models. This coupling has been demonstrated in
particular between structural and aerodynamic computations [e.g. see 14,15] but
also between structural response and temperature distribution [16,17]. These
strong features of reduced order models allow the consideration and study of
interaction problems that, while possible with full order models, are
computationally very extensive.
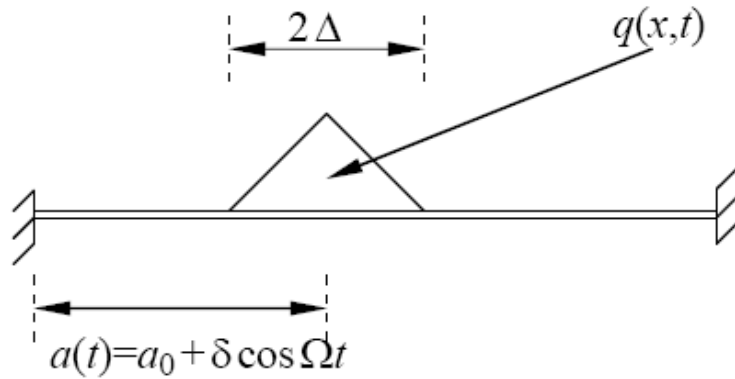
Figure 1. Model problem for the analysis of the thermal effects of
an oscillating shock.

One such problem, considered here in detail, is the effects that shock oscillations have on the response of the panels on which they are attached. In addition to the fluctuations in pressure and aerodynamic forces, the oscillation of the shock is also expected to induce a similar oscillation of the heat flux, the effect of which is poorly understood. Accordingly, it is desired here to address this problem within the context of thermal and structural ROMs, see [16,17], including in particular a parametric study with respect to the frequency of the flux oscillations. This problem is investigated here on a beam model (see Fig. 1) of a panel which is clamped at both ends and is subjected to the combined effect of (i) a distribution of heat flux that is localized at one point of the beam with that point oscillating along the beam at a constant frequency Ω and (ii) an impinging acoustic wave.

Furthermore, due to the extreme heating conditions of hypersonic vehicles (temperatures over 3,000 °F are to be expected [18]), some of the material properties will change throughout the flight envelope. In order for reduced order models to truly capture the response of these vehicle panels it is necessary to

model the properties of the panel material as they change with temperature. Accordingly, one objective of this research is to extend the thermal-structural reduced order modeling strategy to include the variations with temperature, assumed linear, of the elasticity tensor and the coefficient of thermal expansion. The linearity assumption appears well supported over a notable temperature range by experimental data suggesting that the Young's modulus and coefficient of thermal expansion do vary linearly while the Poisson's ratio appears approximately independent of temperature.

CHAPTER 2 – REDUCED ORDER MODEL FORMULATION

2.1 Thermal and Structural Governing Equations

As described in the previous section, a primary objective of the present investigation was the extension of the combined thermal-structural reduced order modeling approach to include the variations of the structural properties, most notably the elasticity tensor and the coefficient of thermal expansion, with temperature. This section which details the derivation of this extension is based on the approach formulated in [16,17].

It is desired here to represent both temperature and displacement fields in a "modal expansion" form, i.e. as

$$T(\underline{X},t) = \sum_{n=1}^{\mu} \tau_n(t)\, T^{(n)}(\underline{X}) \tag{1}$$

for the temperature, and

$$u_i(\underline{X},t) = \sum_{n=1}^{M} q_n(t)\, U_i^{(n)}(\underline{X}) \tag{2}$$

for the displacement. In these equations, the functions $U_i^{(m)}$ and $T^{(m)}$ are specified functions of the position vector $\underline{X}$ in the *undeformed* configuration, chosen to satisfy the necessary boundary conditions.

To obtain a set of (nonlinear) ordinary differential equations governing the evolution of the generalized coordinates $q_n(t)$ and $\tau_n(t)$, it is first necessary to derive the governing field equations for the displacements $u_i(\underline{X},t)$ and

temperature $T(\underline{X},t)$ in the undeformed configuration. Following references [19-21], one obtains (see also [7,16,17])

$$\frac{\partial}{\partial X_k}\left(F_{ij}\,S_{jk}\right)+\rho_0\,b_i^0 = \rho_0\,\ddot{u}_i \qquad \text{for } \underline{X} \in \Omega_0 \tag{3}$$

where $\underline{\underline{S}}$ denotes the second Piola-Kirchhoff stress tensor, ρ_0 is the density in the reference configuration, and $\underline{b}^0$ is the vector of body forces, all of which are assumed to depend on the coordinates X_i of the undeformed configuration in which the structure occupies the domain Ω_0. Further, in Eq. (3), the deformation gradient tensor $\underline{\underline{F}}$ is defined by its components F_{ij} as

$$F_{ij} = \frac{\partial x_i}{\partial X_j} = \delta_{ij} + \frac{\partial u_i}{\partial X_j} \tag{4}$$

where δ_{ij} denotes the Kronecker symbol and the displacement vector is $\underline{u} = \underline{x} - \underline{X}$, $\underline{x}$ being the position vector in the deformed configuration.

The heat conduction equation on the domain Ω_0 can be written as

$$\rho_0\,T\,\dot{s} = \frac{\partial}{\partial X_i}\left[k_{ij}^0\,\frac{\partial T}{\partial X_j}\right] \tag{5}$$

where s denotes the specific entropy and $\underline{\underline{k}}^0$ denotes the conductivity tensor pulled back to the undeformed configuration according to

$$\underline{\underline{k}}^0 = \det\!\left(\underline{\underline{F}}\right)\underline{\underline{F}}^{-1}\,\underline{\underline{k}}\,\underline{\underline{F}}^{-T} \tag{6}$$

where $\underline{\underline{k}}$ is the conductivity tensor in the deformed configuration.

To complete the formulation of the problem, it is necessary to define the material constitutive relations which stem from the Helmholtz free energy (per unit mass) $\mathcal{F}$ defined as

$$\mathcal{F} = \mathcal{E} - T \, \mathcal{S} \tag{7}$$

where $\mathcal{E}$ denotes the elastic energy. Specifically, one has

$$\rho_0 \left(\frac{\partial \mathcal{F}}{\partial E_{ij}} \right)_T = S_{ij} \quad \text{and} \quad \left(\frac{\partial \mathcal{F}}{\partial T} \right)_{E_{ij}} = -\mathcal{S} \tag{8),(9}$$

where $\underline{\underline{E}}$ denotes the Green strain tensor, i.e.

$$E_{ij} = \frac{1}{2} \left(F_{ki} \, F_{kj} - \delta_{ij} \right). \tag{10}$$

Key in the present effort is the form of the Helmholtz free energy which is assumed to represent the material. The Duhamel-Neumann form of the Helmholtz free energy [19] is traditionally assumed, especially when the temperature variations of the elastic properties are neglected. Specifically, it is postulated that

$$\rho_0 \, \mathcal{F} = \frac{1}{2} \, C_{ijkl} \, E_{ij} \, E_{kl} - C_{ijkl} \alpha_{kl} \, (T - T_0) \, E_{ij} + f(T, T_0) \tag{11}$$

where $\underline{\underline{C}}$ denotes the fourth order elasticity tensor, $\underline{\underline{\alpha}}$ the second order tensor of thermal expansion, T_0 is the reference temperature, and [19]

$$f(T, T_0) = -\rho_0 \, C_v \, T_0 \left[\frac{T}{T_0} \ln \left(\frac{T}{T_0} \right) - \frac{T}{T_0} + 1 \right] \tag{12}$$

in which C_v is the specific heat per unit mass measured in the state of constant strain.

The stress-strain relation is then obtained from Eq. (8) as

$$S_{ij} = \rho_0 \left(\frac{\partial \mathcal{F}}{\partial E_{ij}} \right)_T = C_{ijkl} \left[E_{kl} - \alpha_{kl} \left(T - T_0 \right) \right] \tag{13}$$

whether the material properties (i.e. C_{ijkl} and α_{ij}) depend on temperature or not.

The governing equation for the heat convection is then obtained by combining Eq. (5) and (9). Specifically, gives the rate of change of the entropy as

$$\dot{S} = -\frac{\partial^2 \mathcal{F}}{\partial E_{ij} \, \partial T} \dot{E}_{ij} - \frac{\partial^2 \mathcal{F}}{\partial^2 T} \dot{T} \, . \tag{14}$$

or, assuming C_v to be constant

$$
\begin{aligned}
\dot{S} = &\frac{1}{\rho_0} \left[C_{ijkl} \alpha_{kl} \, \dot{E}_{ij} \right] + \frac{C_v}{T} \dot{T} + \frac{1}{\rho_0 T} \left[\left(\frac{\partial \alpha_{ij}}{\partial T} \left(T - T_0 \right) - \frac{\partial C_{ijkl}}{\partial T} E_{kl} \right) \dot{E}_{ij} \right] \\
&+ \frac{1}{\rho_0 T} \left[\frac{1}{2} \frac{\partial^2 C_{ijkl}}{\partial T^2} E_{ij} \, E_{kl} - \frac{\partial^2 \alpha_{ij}}{\partial T^2} \left(T - T_0 \right) E_{ij} - 2 \frac{\partial \alpha_{ij}}{\partial T} E_{ij} \right] \dot{T}
\end{aligned}
\tag{15}
$$

Note that this complex expression reduces to the first two terms, appearing in [16,17], when the elasticity tensor and coefficient of thermal expansion are independent of temperature. Combining Eqs (5) and (15) yields finally the desired heat conduction equation

$$\rho_0 \, C_v \frac{\partial T}{\partial t} - \frac{\partial}{\partial X_i} \left(k_{ij}^0 \frac{\partial T}{\partial X_j} \right) = -T \, \alpha_{ij} \frac{\partial E_{ij}}{\partial t} + G \tag{16}$$

where G denotes a series of terms involving the derivatives of C_{ijkl} and α_{ij}. Specifically,

$$G = \left(\frac{\partial \alpha_{ij}}{\partial T} (T - T_0) - \frac{\partial C_{ijkl}}{\partial T} E_{kl} \right) \frac{\partial E_{ij}}{\partial t} +$$

$$\left[\frac{1}{2} \frac{\partial^2 C_{ijkl}}{\partial T^2} E_{ij} E_{kl} - \frac{\partial^2 \alpha_{ij}}{\partial T^2} (T - T_0) E_{ij} - 2 \frac{\partial \alpha_{ij}}{\partial T} E_{ij} \right] \dot{T} \tag{17}$$

The terms lumped in G can be considered as an additional latency effect, beside the first term on the right-hand-side of Eq. (16), as they all involve the strain. They differ from the classical term (the first term on the right-hand-side of Eq. (16)) by their dependence on the variations of the structural properties with temperature.

The derivation of the governing equations for the generalized coordinates $q_n(t)$ and $\tau_n(t)$ is then achieved by introducing Eqs (1) and (2) in Eqs (3), (4), (10), (13), (16) and (17) and proceeding with a Galerkin approach. This process leads to the differential equations

$$M_{ij} \ddot{q}_j + D_{ij} \dot{q}_j + K_{ij}^{(1)} q_j - K_{ijl}^{(th)} q_j \tau_l +$$

$$K_{ijl}^{(2)} q_j q_l + K_{ijlp}^{(3)} q_j q_l q_p = F_i + F_{il}^{(th)} \tau_l \tag{18}$$

and

$$B_{ij} \dot{\tau}_j + \tilde{K}_{ij} \tau_j + K_{ijl}^{(st)} \dot{q}_j \tau_l = P_i + R_{ij} \tau_j. \tag{19}$$

Considering in particular the structural reduced order model, note that the coefficients $K_{ij}^{(1)}$, $K_{ijl}^{(2)}$, and $K_{ijlp}^{(3)}$ are given as [16]

$$K_{mn}^{(1)} = \int_{\Omega_0} \frac{\partial U_i^{(m)}}{\partial X_k} C_{iklp} \frac{\partial U_l^{(n)}}{\partial X_p} d\underline{X} \tag{20}$$

8

$$K_{mnp}^{(2)} = \frac{1}{2}\left[\hat{K}_{mnp}^{(2)} + \hat{K}_{pmn}^{(2)} + \hat{K}_{npm}^{(2)}\right]$$ (21)

$$\hat{K}_{mnp}^{(2)} = \int_{\Omega_0} \frac{\partial U_i^{(m)}}{\partial X_j} C_{ijkl} \frac{\partial U_r^{(n)}}{\partial X_k} \frac{\partial U_r^{(p)}}{\partial X_l} d\underline{X}$$ (22)

$$K_{msnp}^{(3)} = \frac{1}{2}\int_{\Omega_0} \frac{\partial U_i^{(m)}}{\partial X_j} \frac{\partial U_i^{(s)}}{\partial X_k} C_{jklw} \frac{\partial U_r^{(n)}}{\partial X_l} \frac{\partial U_r^{(p)}}{\partial X_w} d\underline{X} .$$ (23)

Clearly, these coefficients implicitly depend on the temperature distribution since they are linearly dependent on the tensor C_{ijkl}. Proceeding similarly with the parameters $K_{ijl}^{(th)}$ and $F_{il}^{(th)}$, defined as

$$K_{mnp}^{(th)} = \int_{\Omega_0} \frac{\partial U_i^{(m)}}{\partial X_k} \frac{\partial U_i^{(n)}}{\partial X_j} C_{kjlr}\alpha_{lr}T^{(p)} d\underline{X}$$ (24)

$$F_{mn}^{(th)} = \int_{\Omega_0} \frac{\partial U_i^{(m)}}{\partial X_k} C_{iklp}\alpha_{lp}T^{(n)} d\underline{X}$$ (25)

demonstrates that they are also temperature distribution dependent since they involve the product $C_{ijkl}\,\alpha_{kl}$. These findings notably complicate the reduced order modeling formulation as they imply that new coefficients would have to be recomputed at every time step if the temperature distribution changes with time. This difficulty can be bypassed by assuming a polynomial dependence of C_{ijkl} and α_{ij} on the temperature. For example, assuming this dependence being linear, one has

$$C_{ijkl} = C_{ijkl}^{(0)} - C_{ijkl}^{(1)}\,T$$ (26)

9

and

$$\alpha_{ij} = \alpha_{ij}^{(0)} - \alpha_{ij}^{(1)} T. \tag{27}$$

When propagating the temperature dependence through the terms in Eqs (20) and

(24), it becomes more convenient to combine the expressions of $K_{ij}^{(1)}$ and $K_{ij,l}^{(th)}$ in

order to determine a single expression for the linear stiffness coefficient's

dependence on temperature. Following the substitution of Eqs (26) and (27) into

Eqs (20)-(25) demonstrates that the coefficients, $K_{ijl}^{(2)}$, and $K_{ijlp}^{(3)}$ would be linear

in the thermal generalized coordinates τ_i, while $K_{ij}^{(1)}$ and $F_i^{(th)}$ would be cubic

in these variables, as

$$K_{ij}^{(1)} = K_{ij,0}^{(1)} - K_{ij,l}^{(1)} \tau_l - K_{ij,lm}^{(1)} \tau_l \tau_m - K_{ij,lmn}^{(1)} \tau_l \tau_m \tau_n \tag{28}$$

$$K_{ijl}^{(2)} = K_{ijl,0}^{(2)} - K_{ijl,r}^{(2)} \tau_r \tag{29}$$

$$K_{msnp}^{(3)} = K_{msnp,0}^{(3)} - K_{msnp,l}^{(3)} \tau_l \tag{30}$$

$$F_i^{(th)} = -F_{i,l}^{(th)} \tau_l - F_{i,lr}^{(th)} \tau_l \tau_r - F_{i,lrs}^{(th)} \tau_l \tau_r \tau_s. \tag{31}$$

where

$$K_{mn,0} = \int_{\Omega_0} \frac{\partial U_i^{(m)}}{\partial X_k} C_{iklp}^{(0)} \frac{\partial U_l^{(n)}}{\partial X_p} d\underline{X} \tag{32}$$

$$K_{mn,r} = -\int_{\Omega_0} \left[\frac{\partial U_j^{(m)}}{\partial X_K} \frac{\partial U_j^{(n)}}{\partial X_i} C_{iklp}^{(o)} \alpha_{lp}^{(0)} T^{(r)} - \frac{\partial U_i^{(m)}}{\partial X_K} C_{iklp}^{(1)} \frac{\partial U_l^{(n)}}{\partial X_p} T^{(r)} \right] d\underline{X} \tag{33}$$

$$K_{mn,rs} = \int\limits_{\Omega_0} \frac{\partial U_j^{(m)}}{\partial X_K} \frac{\partial U_j^{(n)}}{\partial X_i} \left[C_{iklp}^{(0)} \alpha_{lp}^{(1)} T^{(r)} T^{(s)} + C_{iklp}^{(1)} \alpha_{lp}^{(0)} T^{(r)} T^{(s)} \right] d\underline{X} \qquad (34)$$

$$K_{mn,rsg} = -\int\limits_{\Omega_0} \frac{\partial U_j^{(m)}}{\partial X_k} \frac{\partial U_j^{(n)}}{\partial X_i} C_{iklp}^{(1)} \alpha_{lp}^{(1)} T^{(r)} T^{(s)} T^{(g)} d\underline{X} \qquad (35)$$

$$K_{mnp} = \frac{1}{2}\left[\hat{K}_{mnp} + \hat{K}_{pmn} + \hat{K}_{npm} \right] \qquad (36)$$

$$\hat{K}_{mnp} = \int\limits_{\Omega_0} \frac{\partial U_i^m}{\partial X_j} C_{ijkl}^{(0)} \frac{\partial U_r^{(n)}}{\partial X_k} \frac{\partial U_r^{(p)}}{\partial X_l} d\underline{X} \qquad (37)$$

$$K_{mnp,g} = \frac{1}{2}\left[\hat{K}_{mnp,g} + \hat{K}_{pmn,g} + \hat{K}_{npm,g} \right] \qquad (38)$$

$$\hat{K}_{mnp,g} = \int\limits_{\Omega_0} \frac{\partial U_i^{(m)}}{\partial X_j} C_{ijkl}^{(1)} T^{(g)} \frac{\partial U_r^{(n)}}{\partial X_k} \frac{\partial U_r^{(p)}}{\partial X_l} d\underline{X} \qquad (39)$$

$$K_{msnp} = \frac{1}{2}\int\limits_{\Omega_0} \frac{\partial U_i^{(m)}}{\partial X_j} \frac{\partial U_i^{(s)}}{\partial X_k} C_{jklw}^{(0)} \frac{\partial U_r^{(n)}}{\partial X_l} \frac{\partial U_r^{(p)}}{\partial X_w} d\underline{X} \qquad (40)$$

$$K_{msnp,g} = \frac{1}{2}\int\limits_{\Omega_0} \frac{\partial U_i^{(m)}}{\partial X_j} \frac{\partial U_i^{(s)}}{\partial X_k} C_{jklw}^{(1)} T^{(g)} \frac{\partial U_r^{(n)}}{\partial X_l} \frac{\partial U_r^{(p)}}{\partial X_w} d\underline{X} \qquad (41)$$

$$F_{m,n} = -\int\limits_{\Omega_0} \frac{\partial U_i^{(m)}}{\partial X_k} C_{iklr}^{(0)} \alpha_{lr}^{(0)} T^{(n)} d\underline{X} \qquad (42)$$

$$F_{m,ng} = \int\limits_{\Omega_0} \frac{\partial U_i^{(m)}}{\partial X_k} \left[C_{iklr}^{(0)} \alpha_{lr}^{(1)} + C_{iklr}^{(1)} \alpha_{lr}^{(0)} \right] T^{(n)} T^{(g)} d\underline{X} \qquad (43)$$

$$F_{m,ngh} = -\int\limits_{\Omega_0} \frac{\partial U_i^{(m)}}{\partial X_k} C_{iklr}^{(1)} \alpha_{lr}^{(1)} T^{(n)} T^{(g)} T^{(h)} d\underline{X} \qquad (44)$$

11

In Eq. (19), B_{ij} and $\tilde{K}_{ij}$ are the elements of the capacitance and

conductance matrices of the reduced order model and $K_{ijl}^{(st)}$ is a linear latency

term, dual of $K_{ijl}^{(th)}$. Further, the term P_i denotes the source term associated with

the boundary conditions and the external flux while R_{ij} involves latency and

change of geometry effects [16]. $K_{ijl}^{(st)}$ and R_{ij} are the terms in the heat

conduction equation that are dependent on the temperature distribution. They also

represent the feedback effect of the structural deformations on the temperature

distribution. This effect is generally recognized as small for small to medium

deformations and thus $K_{ijl}^{(st)}$ and R_{ij} will be neglected in the present analysis.

Their dependence on the temperature distribution is thus not analyzed further.

2.2 Basis Selection

The integral expressions for all coefficients, see Eqs (20)-(25) for Eq. (18),

demonstrate, as expected, their dependence on the selection of the basis functions

$\underline{U}_i^{(m)}$ and $\underline{T}^{(i)}$ which represents a key step in the formulation of the reduced

order modeling strategy. Following the discussions of [7,8,16], the former were

selected as the linear modes of the structure that would appear significantly in the

linear response appended of an ensemble of "dual modes" that are obtained as

specific nonlinear static solutions (see [7] for an extended presentation and

validation in isothermal conditions). An enrichment of this structural basis by one

12

or several problem-specific functions may also be warranted, e.g. see the first validation case. Note that this basis is temperature independent, i.e. evaluated for a specific temperature distribution.

The thermal basis functions, $T^{(m)}(\underline{X})$ used in the steady validation cases [16,17] will be adopted again in the present study. They were constructed as the product of a function of the through thickness coordinate z by a function of the remaining two coordinates $(=\underline{X}_p)$. That is,

$$T^{(m)}(\underline{X}) = T_t^{(m)}(z) T_p^{(m)}(\underline{X}_p). \tag{45}$$

The function $T_t^{(m)}(z)$ was selected as the temperature distribution satisfying the 1-D steady heat conduction equation through the thickness. Further, two sets of functions $T_p^{(m)}(\underline{X}_p)$ were combined to represent the inplane variation of temperature. The first group of functions, $T_{p,BC}^{(m)}(\underline{X}_p)$, were selected, e.g. as linear functions, to homogenize the boundary conditions on temperature. To this set were added the functions $T_{p,eig}^{(m)}(\underline{X}_p)$ which were computed as the eigenvectors of the linear finite element approximation of the time-dependent heat conduction problem on the top and bottom surfaces, i.e. spanned by $\underline{X}_p$.

2.3 Identification of the Parameters of the Structural Reduced Order Model

2.3.1 No Temperature Present

While Eqs (32)-(44) provide exact expressions for the coefficients of the structural reduced order model, they are not in a form that is convenient for evaluation from a finite element model in which only discretized values of the modes are available. This observation has led, as in prior investigation, to the consideration of *indirect* methods for the estimation of the coefficients from a series of static finite element computations. In the absence of temperature variations, the STEP identification strategy of the coefficients $K_{ij}^{(1)}$, $K_{ijl}^{(2)}$, and $K_{ijlp}^{(3)}$ as initially proposed by Muravyov and Rizzi [22] and modified by [7] has often been utilized. In fact, it is also the basis for the identification approach used in [16] in the presence of temperature and thus is first reviewed here before addressing the identification of the stiffness coefficients in Eq. (18).

The essential idea behind the STEP approach is to impose a series of specified displacement fields to the structure and to determine the forces required to achieve these displacements. Then, from these data, all the above parameters are determined by solving linear algebraic equations.

The first step in the approach is to estimate the parameters $K_{ij}^{(1)}$, $K_{ijj}^{(2)}$, and $K_{ijjj}^{(3)}$, for each value of j. As it can be seen from Eq. (18) a displacement field proportional to a single basis function, i.e.

$$u_i^r(\underline{X}) = q_j^{(r)} U_i^{(j)}(\underline{X}) \qquad r = 1,2,3 \tag{46}$$

14

for each value of j in turn results. Then, the values $q_j^{(r)}$ are constant scaling

factors that are such that the displacements produced are large enough to induce

significant geometric nonlinear effects. From trial and error with different values

of $q_j^{(r)}$ it was determined that a good choice of these values is such that the

resulting displacement field is of approximately between one tenth and one

thickness of the structure. With this in mind, Eq. (18) reduces to

$$K_{ij}^{(1)} q_j^{(r)} + K_{ijj}^{(2)} q_j^{(r)2} + K_{ijjj}^{(3)} q_j^{(r)3} = F_i^{(r)} \qquad r = 1,2,3 \qquad (47)$$

where the force terms $F_i^{(r)}$ are computed from the traction predicted in each case

by a finite element analysis (e.g., MSC.Nastran). Then, these relations represent a

set of 3 equations in which the only unknowns are the 3 parameters $K_{ij}^{(1)}$, $K_{ijj}^{(2)}$,

and $K_{ijjj}^{(3)}$, which appear linearly.

The second step of the identification procedure is the estimation of the

parameters $K_{ijl}^{(2)}$, $K_{ijll}^{(3)}$, and $K_{ijjl}^{(3)}$ for $l \neq j$. These parameters appear in the

model through the generalized coordinates q_j and q_l. Therefore, they can be

determined following a similar procedure as in the first step but with the

imposition of displacements that are of the form

$$u_i^{(r)}(\underline{X}) = q_j^{(r)} U_i^{(j)}(\underline{X}) + q_l^{(r)} U_i^{(l)}(\underline{X}) \qquad r = 1,2,3. \qquad (48)$$

Finally, the third and last step of the identification procedure is the

determination of the parameters $K_{ijlp}^{(3)}$ for j, l, and p all different. In this case, the

15

displacement field needed in order to determine the parameters of interest is of the following form.

$$u_i(\underline{X}) = q_j U_i^{(j)}(\underline{X}) + q_l U_i^{(l)}(\underline{X}) + q_p U_i^{(p)}(\underline{X}) \tag{49}$$

Lastly, the remaining parameters of the model of Eq. (18), i.e. the modal masses M_{ij}, damping coefficients D_{ij}, and modal forces F_i are determined from the finite element model of the structure as follows

$$M_{ij} = \underline{U}^{(i)T} \underline{\underline{M}}_{FE} \underline{U}^{(j)} \tag{50}$$

$$D_{ij} = \underline{U}^{(i)T} \underline{\underline{D}}_{FE} \underline{U}^{(j)} \tag{51}$$

$$F_i = \underline{U}^{(i)T} \underline{F}_{FE} \tag{52}$$

$$F_{il}^{(th)} = \underline{U}^{(i)T} \underline{\underline{F}}_{FE}^{(th)} \tag{53}$$

where $\underline{\underline{M}}_{FE}, \underline{\underline{D}}_{FE}$, and $\underline{F}_{FE}$ are the global mass matrix, damping matrix, and forces applied to the full finite element model. Further, $\underline{\underline{F}}_{FE}^{(th)}$ is the force induced by each temperature variation of the form $1 \times \underline{T}^{(m)}$.

Note finally, that the modal forces F_i will in general be affected by the "pull back" operation. However, this issue was not addressed here because the displacements of the beams and panels considered in this investigation did not exceed a few thicknesses.

2.3.2 Present Model

In order to determine the temperature dependent terms given in Eqs (28)-(31), a method similar to the one specified above will be used. A series of temperature fields, which will result from combinations of thermal modes, will be imposed on the system, and the desired stiffness and force terms will be acquired using the methodology specified above. A system of linear equations will result in which the temperature dependent parameters of Eqs (28)-(31) will be solved for.

In all these equations, the terms with a subscript of 0 denote parameters that are not connected to the thermal generalized coordinates. These terms are found using the method described in Section 2.3.1, in which a uniform temperature field of $0°$ C is enforced on the structure, with the elasticity tensor being independent of temperature and the coefficient of thermal expansion being equal to zero.

As seen in Eqs (29)-(30) the cubic and quadratic stiffness terms depend linearly on temperature, due to the presence of the elasticity tensor. Looking specifically at the quadratic stiffness, Eq. (29) can be rearranged as follows:

$$\left(K_{ijl}^{(2)} - K_{ijl,0}^{(2)} \right) = K_{ijl,r}^{(2)} \tau_r \tag{54}$$

In order to determine the value of $K_{ijl,r}^{(2)}$, temperature fields proportional to each thermal mode as

$$T(\underline{X}) = \tau_r T^{(r)}(\underline{X}) \tag{55}$$

are imposed on the structure, with the elasticity tensor varying with temperature.

With each temperature field applied, the method described in the previous section was applied in order to find $K_{ijl}^{(2)}$. Since τ_r is a known scalar value, the only unknown left is $K_{ijl,r}^{(2)}$, which is directly solved for. In the same way, the terms that define the cubic stiffness coefficient, $K_{ijlp,r}^{(3)}$, can be found.

The linear stiffness coefficients and thermal moment terms have a cubic dependence on temperature. Further, they can be rearranged to have the same form as specified in Eq. (47) but with the thermal generalized coordinates τ_j as opposed to their structural counterparts q_j, e.g.

$$\left(K_{ij}^{(1)} - K_{ij,0}^{(1)} \right) = -K_{ij,l}^{(1)} \tau_l - K_{ij,lm}^{(1)} \tau_l \tau_m - K_{ij,lmn}^{(1)} \tau_l \tau_m \tau_n \ . \tag{56}$$

Based on the similarity between Eqs (47) and (56), temperature fields will now be applied as the displacement fields were applied in the previous section. Thus, the first step is to estimate the parameters $K_{ij,l}^{(1)}$, $K_{ij,ll}^{(1)}$, and $K_{ij,lll}^{(1)}$. Applying a temperature field proportional to a single thermal basis function, i.e.

$$T^{(r)}\left(\underline{X}\right) = \tau_l^{(r)} T^{(l)}\left(\underline{X}\right) \qquad r = 1,2,3 \tag{57}$$

for each value of l in turn results in

$$\left(K_{ij}^{(1)} - K_{ij,0}^{(1)} \right) = -K_{ij,l}^{(1)} \tau_l - K_{ij,ll}^{(1)} \tau_l \tau_l - K_{ij,lll}^{(1)} \tau_l \tau_l \tau_l \tag{58}$$

As each temperature field is applied to the system, which has both the elasticity tensor and the coefficient of thermal expansion varying linearly with temperature, the method described in 2.3.1 is again applied in order to determine $K_{ij}^{(1)}$. Since

18

τ_l is a known scalar, what results is a system of 3 linear equations in which there are 3 unknowns, $K_{ij,l}^{(1)}$, $K_{ij,ll}^{(1)}$, and $K_{ij,lll}^{(1)}$.

The next step is the estimation of the parameters $K_{ij,lr}^{(1)}$, $K_{ij,lrr}^{(1)}$, and $K_{ij,llr}^{(1)}$, for $l \neq r$, which appear in the model through the generalized coordinates τ_r and τ_l. These parameters can be found following a similar procedure as the first step but with the application of the temperature fields that are of the form

$$T^{(p)}(\underline{X}) = \tau_l^{(p)} T^{(l)}(\underline{X}) + \tau_r^{(p)} T^{(r)}(\underline{X}) \qquad p = 1,2,3. \tag{59}$$

The third and last step involves the determination of the parameters $K_{ij,lrs}^{(3)}$, for l, r, and s all different. The temperature field imposed on the system in order to find this parameter is of the following form.

$$T(\underline{X}) = \tau_l T^{(l)}(\underline{X}) + \tau_r T^{(r)}(\underline{X}) + \tau_s T^{(s)}(\underline{X}) \tag{60}$$

The temperature dependent parameters of Eq. (31), which describes the thermal moment term, can be found in the same manner.

CHAPTER 3 – REDUCED ORDER MODEL VALIDATION

The first purpose of the current investigation is to create a thermal

structural reduced order model that accurately predicts the motion of a beam when

subjected to an oscillating heat source and acoustic loading. This model does not

incorporate temperature dependent material properties, which means that the

coefficients identified by Eqs (18) and (19) will be used and that these same

equations will be used for the computation of the generalized coordinates. Before

addressing the oscillating flux problem, it was desired to first validate the thermal

and structural reduced order models, both separately and jointly, and this step was

accomplished on the steady problem corresponding to the flux centered on the

beam, i.e. $a_0 = L/2$, $\Omega = 0$, and $\delta = 0$, see Fig. 1 and Table 1. Further, the width

Δ of the triangular heat flux was selected as 0.2*L. Finally, the peak heat flux was

selected so that the peak temperature on the upper surface of the beam would be

10°C while the bottom surface was maintained at 0°C. A no flux boundary

condition was enforced through the thickness at the ends of the beam and a zero

temperature at the ends of the top of the panel. The beam was assumed to be

isotropic with properties given in Table 1 and was modeled by finite elements

using 40 CBEAM elements in MSC.Nastran.

Table 1. Clamped-Clamped Beam Properties

Beam Length (L)	0.2286 m
Cross-section Width (w)	0.0127 m
Cross-section Thickness (h)	7.88 10^{-4} m

Density	2700 kg/m^3
Young's Modulus	73,000 MPa
Shear Modulus	27,730 MPa
Coeff. Thermal Expansion	2.5 10^{-5} /°C
Mesh (CBEAM)	40

3.1 Thermal Reduced Order Model

The validation of the thermal reduced order model was considered first. While the centered steady flux will lead to a symmetric temperature distribution, its oscillating counterpart will not and thus both symmetric and antisymmetric modes were selected. No boundary condition mode was introduced here given the zero temperature boundary condition at the ends of the beam. Further, 10 eigenvectors of the capacitance-conductance generalized eigenvalue problem associated with the 1-D heat conduction on the top surface were considered for the basis. As reviewed above, a linear variation of the temperature through thickness was assumed throughout the length of the beam.

Then, shown in Fig. 2 is a comparison of the temperature distribution computed from Nastran with the one predicted with the 10-mode thermal ROM with a centered, steady heat flux. Figure 3 similarly shows the temperature distribution predicted by Nastran and the 10-mode thermal ROM with a heat flux that is offset to the left by 0.075 beam length, which is the furthest from center that the heat flux will be in a given cycle.
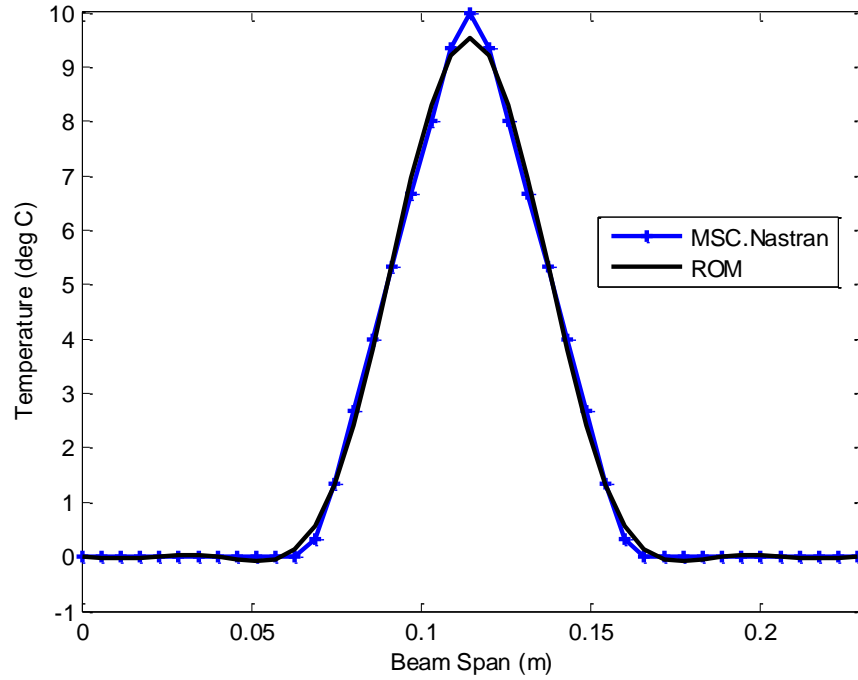
Figure 2. Temperature distribution on top of the beam induced by
the localized steady heat flux. Nastran and reduced order model
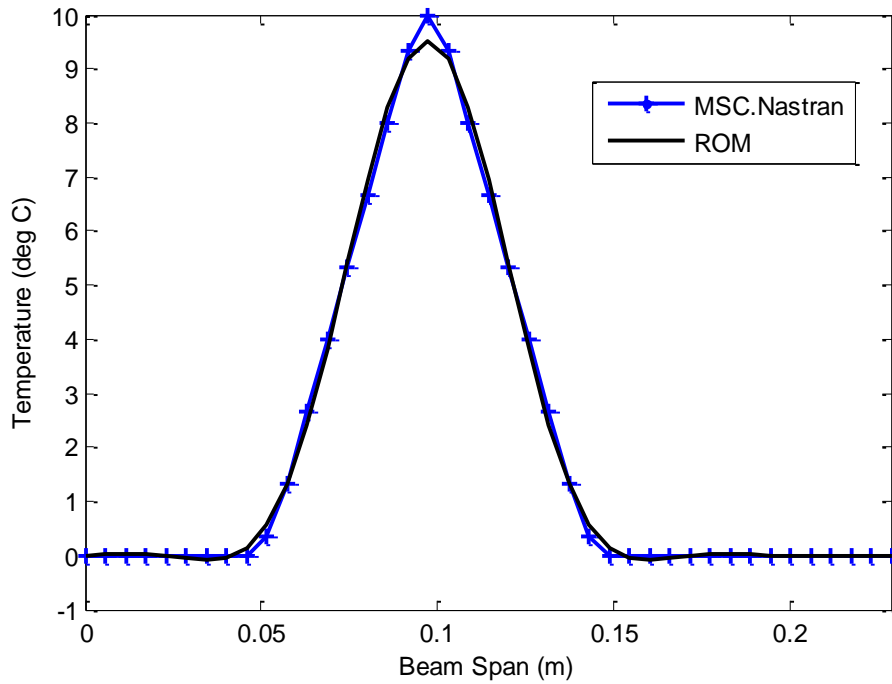steady computations.

Figure 3. Temperature distribution on top of the beam induced by
the localized steady heat flux, offset to the left by 0.075 beam
length. Nastran and ROM steady computations.

The matching is very good although the capturing of the sharp peak is not as accurate. This very localized difference was however found not to induce any noticeable change in structural deflections as will be observed below. Accordingly, no further effort was undertaken to improve the matching of the temperature fields at the peak.

3.2 Structural Reduced Order Model

The structural reduced order modeling was addressed next. A key aspect in obtaining such a model with good predictive capabilities is the selection of the basis to represent the motions. In this regard, note that the temperature distribution of Fig. 2 is not uniform. Thus, a displacement field with both transverse and inplane components is induced through (i) the thermal expansion of part of the beam, and (ii) the compressive effect of the reactions at the clamps. Accordingly, a full field representation approach was adopted here in which both transverse and inplane motions are modeled. Specifically, following [3,4,7,8,13,16,17] the transverse motions will be represented using the corresponding linear modes. The first 7 (4 symmetric and 3 antisymmetric) were selected here based on the frequency range of the acoustic excitation discussed below. Further, 7 dual modes (those with mode 1 dominant, see [7]) were employed for the inplane deformations that are induced by the large transverse deflections. In addition to these deflections, the inplane basis functions must represent well the existing thermal displacements. Since the dual modes are

23

highly focused on representing the transverse-inplane nonlinear coupling, it has

sometimes been necessary (e.g. [16,17]), although not always (e.g. [8]), to enrich

the inplane basis to account for the effect of other loadings (e.g. thermal). Such an

enrichment was found necessary here but no simple, representative thermal

loading scenario (as in [16,17]) could be successfully devised. Accordingly, the 7-

dual mode basis was enriched with the first three inplane linear modes leading to

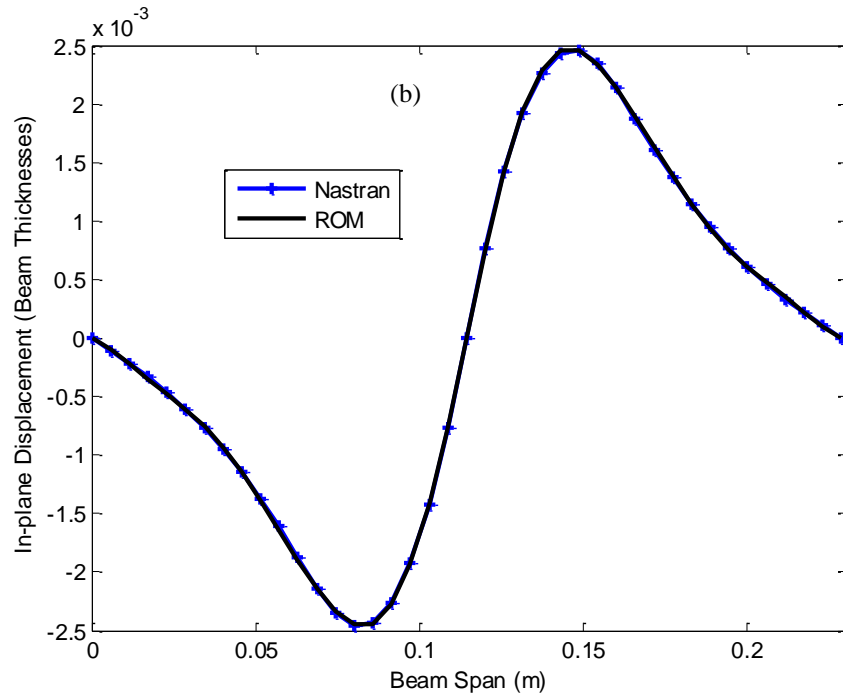a 17-mode structural model, with 7 transverse and 10 inplane modes.
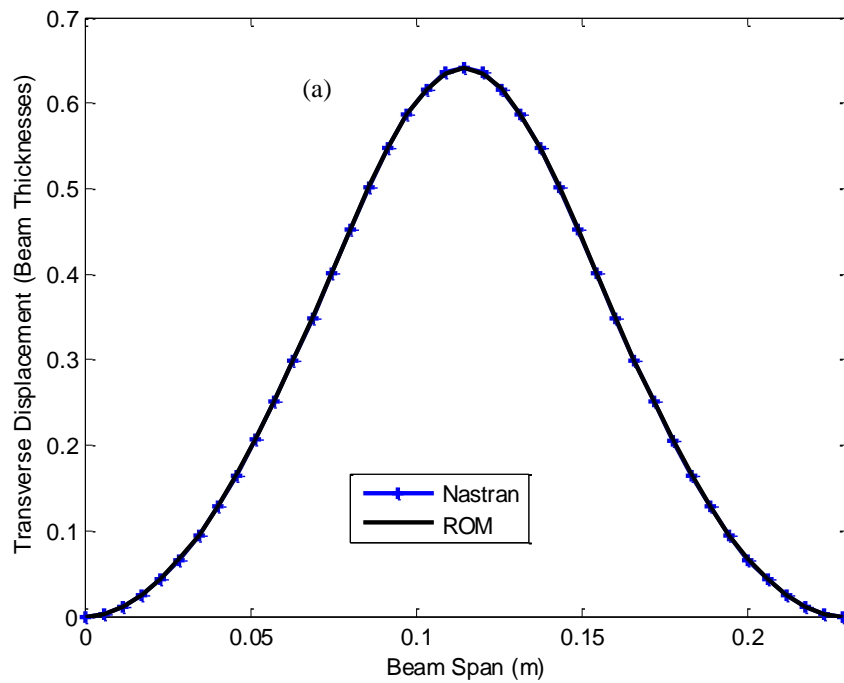
Figure 4. Displacements, (a) transverse, (b) inplane, induced by the localized steady heat flux. ROM and Nastran nonlinear predictions.

Shown in Fig. 4 are the static displacement fields obtained with the reduced order models (both thermal and structural) and full Nastran analyses (both thermal and structural as well) for the centered, steady heat flux. Shown in Fig. 5 are the displacement fields obtained by the reduced order models and Nastran, but with a heat flux that is offset to the left by 0.075 beam length.
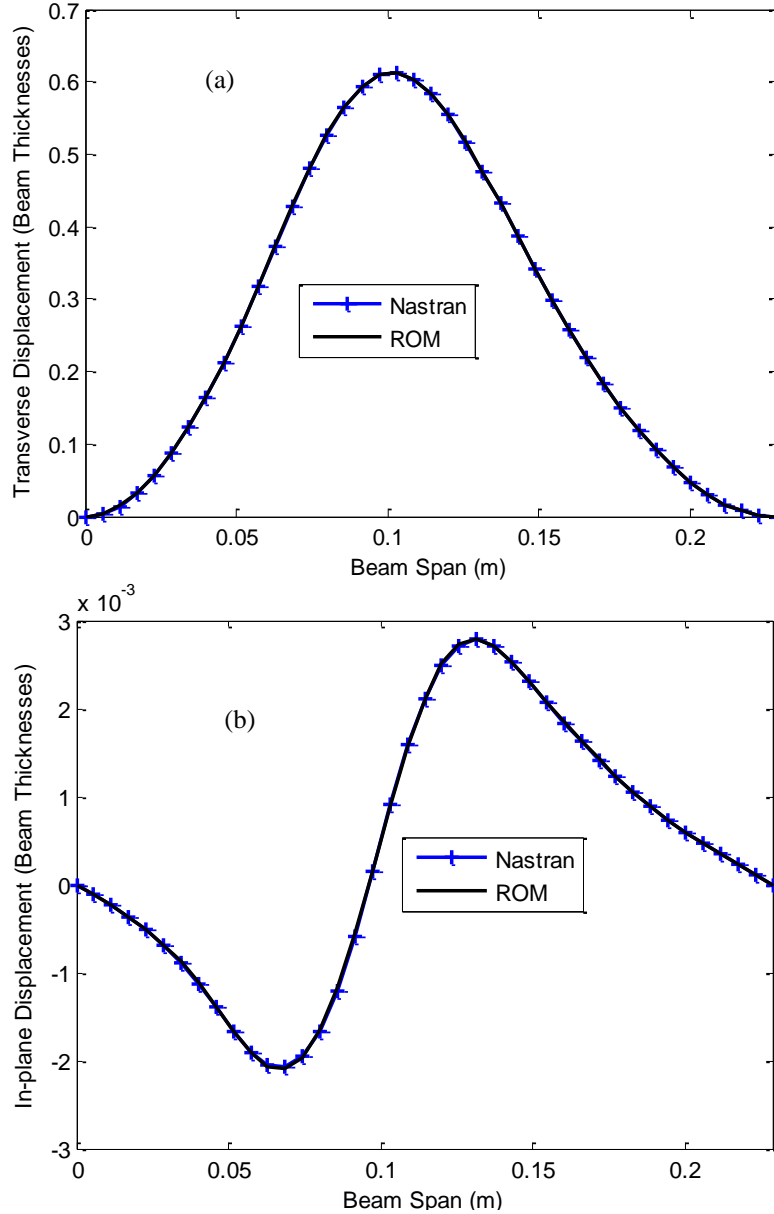
Figure 5. Displacements, (a) transverse, (b) inplane, induced by the localized steady heat flux, offset by 0.075 beam length to the left. ROM and Nastran nonlinear predictions.

The excellent matching obtained supports the appropriateness of the basis.

Shown in Fig. 6 is a similar comparison but for a heat flux 20 times smaller,

leading to a peak temperature of only 0.5°C for which the peak transverse

response is 0.02 thickness. Note in Fig. 6 that both linear and nonlinear analyses

were performed with Nastran and that they differ, albeit only slightly, even for that very small displacement level. This finding may be surprising as it would usually be assumed that the linear theory would be applicable for such small deflections. It is believed that the difference results in fact from the presence of a strong inplane component of the motion which affects nonlinearly the transverse deflections, in the same way an inplane load would.
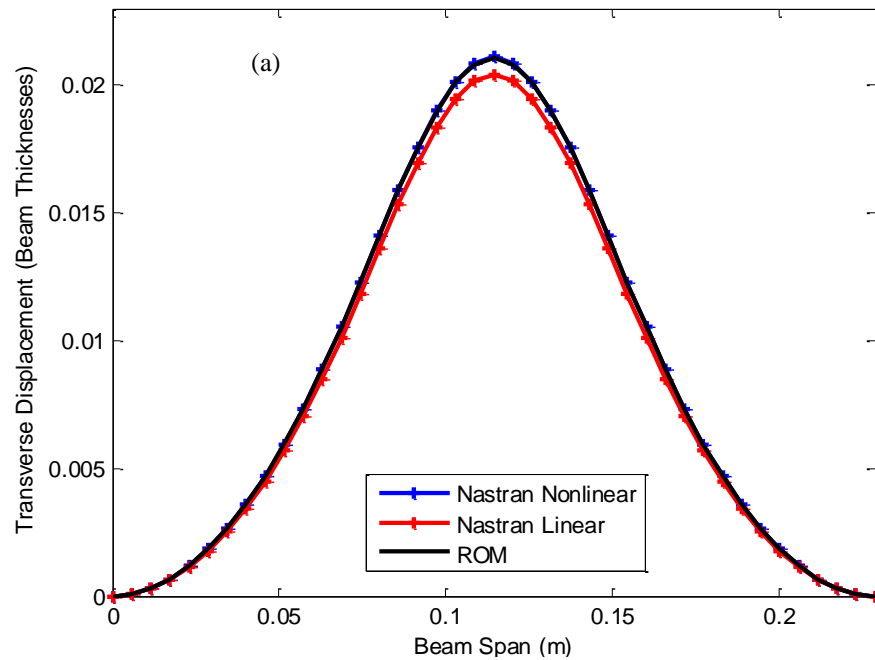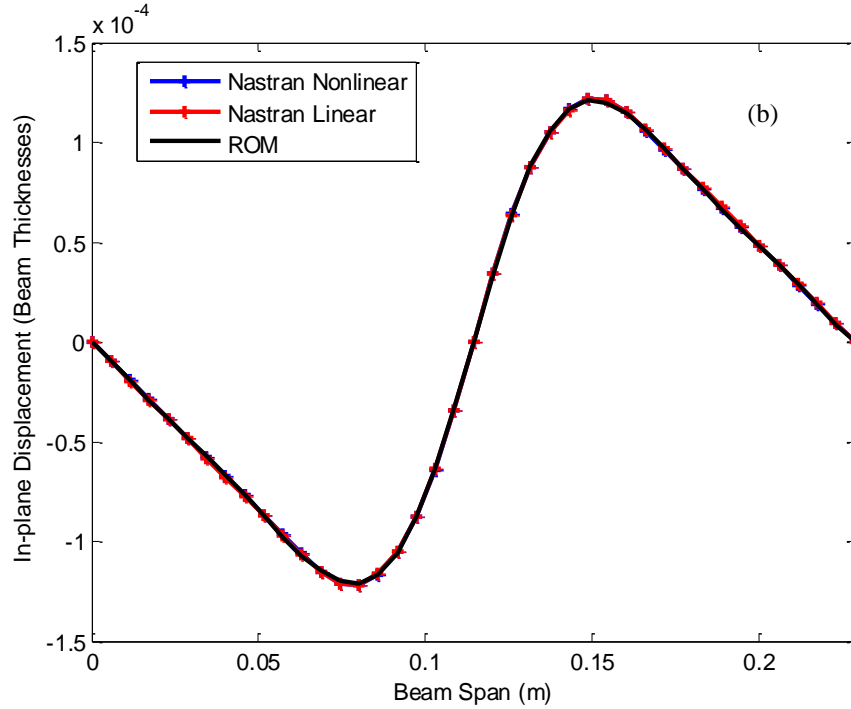
Figure 6. Displacements, (a) transverse, (b) inplane, induced by the localized steady heat flux divided by 20. ROM and Nastran linear and nonlinear predictions.

The final validation of the structural reduced order model focused on its prediction of the dynamic response to an acoustic excitation, modeled here as a uniform pressure varying randomly in time as a white noise bandlimited in the frequency range [0,1042Hz]. Further, three magnitudes of this excitation, measured by the overall sound pressure level (*OASPL* or simply *SPL*), were applied to the beam, in addition to the symmetric temperature loading. At the lowest level, *SPL*=110dB, see Figs 7(a) and 8(a), the transverse response is seen to exhibit only three sharp peaks associated with the symmetric linear transverse modes. At the next level, *SPL*=130dB, see Figs 7(b) and 8(b), the response exhibits many more peaks of frequencies closely matching harmonics/combinations of the linear modes. Further, significant peak broadening

occurs at 145dB in both transverse and inplane spectra due to nonlinearity and peak merging. In the latter, note the significant increase of the response level at the middle of the beam. In fact, the response of the beam to that acoustic excitation and the thermal loading, both symmetric, is no longer symmetric, as it was at the lower excitation levels, *SPL*=110dB and 130dB, note the computationally zero magnitude of the spectra of the inplane displacement on Figs 7(a) and (b). The symmetry breaking at 145dB is only sporadic and was also confirmed from the difference between the transverse responses at the quarter and three-quarter points. In all cases, it is seen that the reduced order models lead to an excellent match of the Nastran predictions.
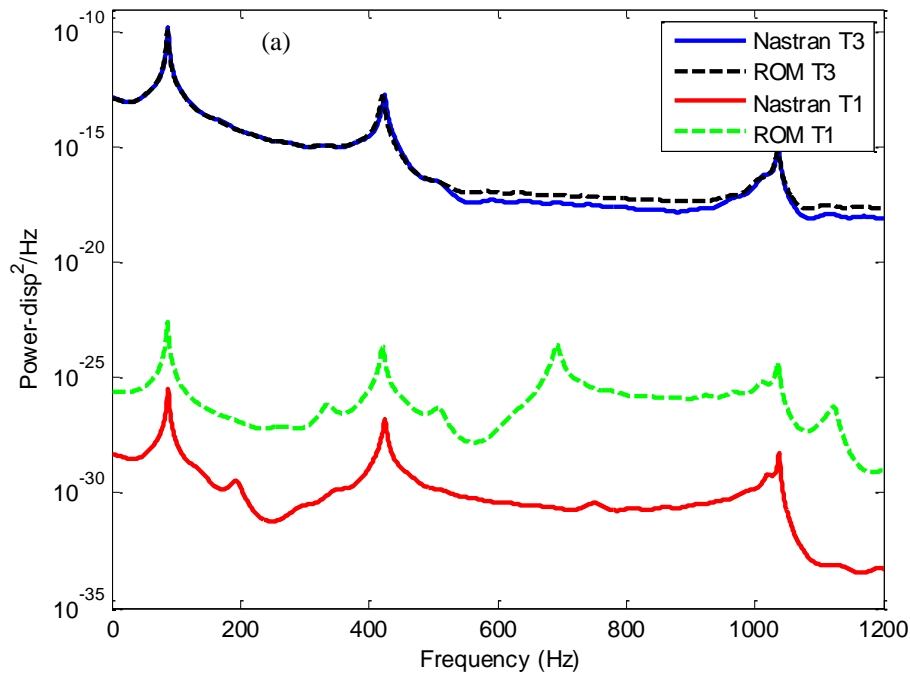
Figure 7. Power spectral density of the transverse (T3) and inplane (T1) deflections at the beam mid point. ROM and Nastran nonlinear predictions. Steady, symmetric heat flux and acoustic excitation of (a) SPL =110dB, (b) SPL =130dB, (c) SPL =145dB.

Figure 8. Power spectral density of the transverse (T3) and inplane (T1) deflections at the beam quarter point. ROM and Nastran nonlinear predictions. Steady, symmetric heat flux and acoustic excitation of (a) *SPL* =110dB, (b) *SPL* =130dB, (c) *SPL* =145dB.

The same acoustic loads were applied again, but with a thermal load that was offset by 0.075 beam thicknesses. The same observations can be made for the offset temperature loading cases as were made for the symmetric thermal and acoustic loading. In particular, the spectra obtained for the lower acoustic loading case, *SPL*=110 dB, see Figs 9(a) and 10(a), show a few sharp peaks, while an *SPL* of 130 dB leads to more peaks matching the harmonics/combinations of the linear modes. Finally, peak broadening occurs at an *SPL* of 145 dB, which is the result of nonlinearity and peak merging. One significant difference between the two thermal loading cases is that there is no symmetry in the offset thermal loading case, which results in a non-zero inplane component for all figures shown. In all cases the matching between the reduced order models and Nastran is excellent.
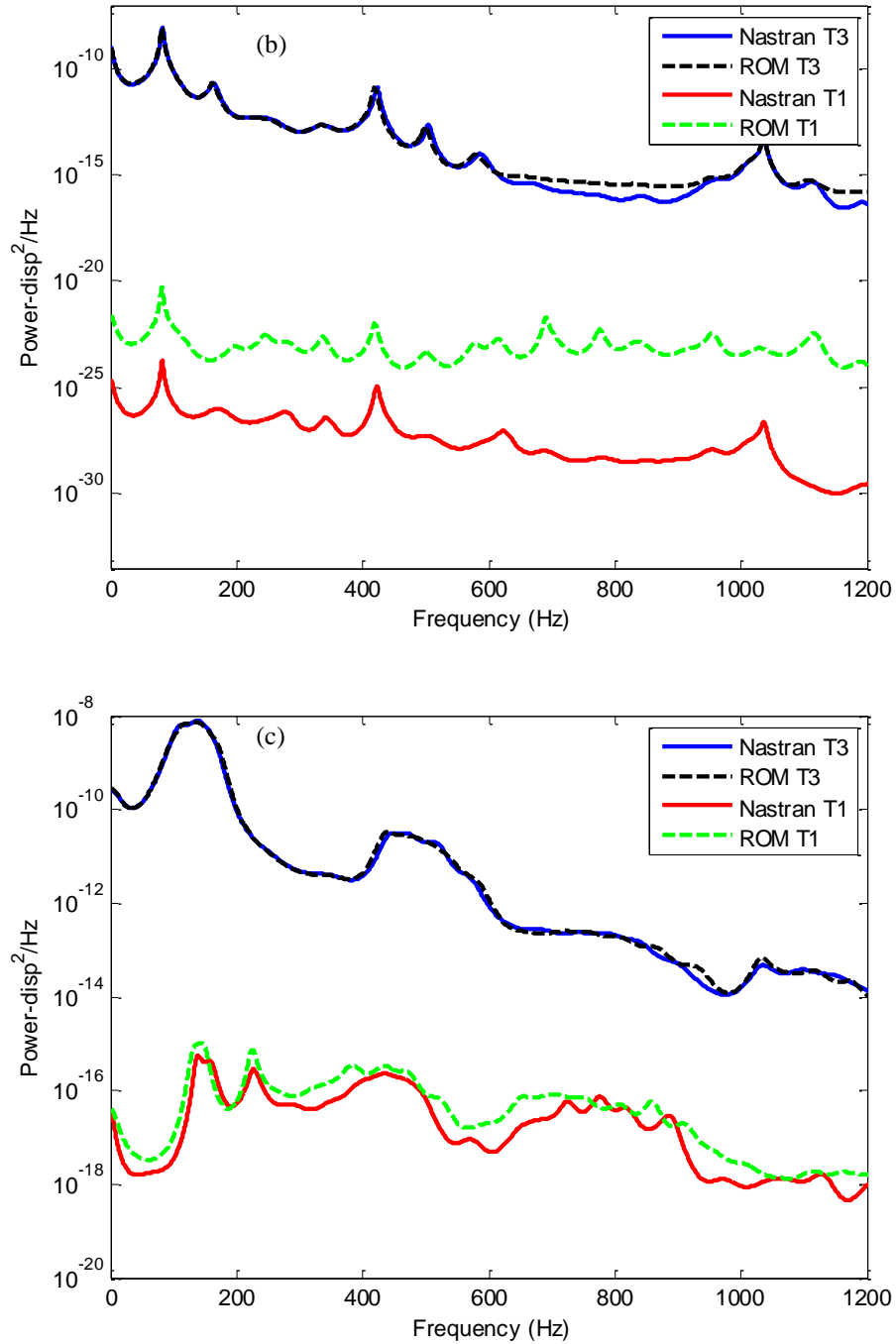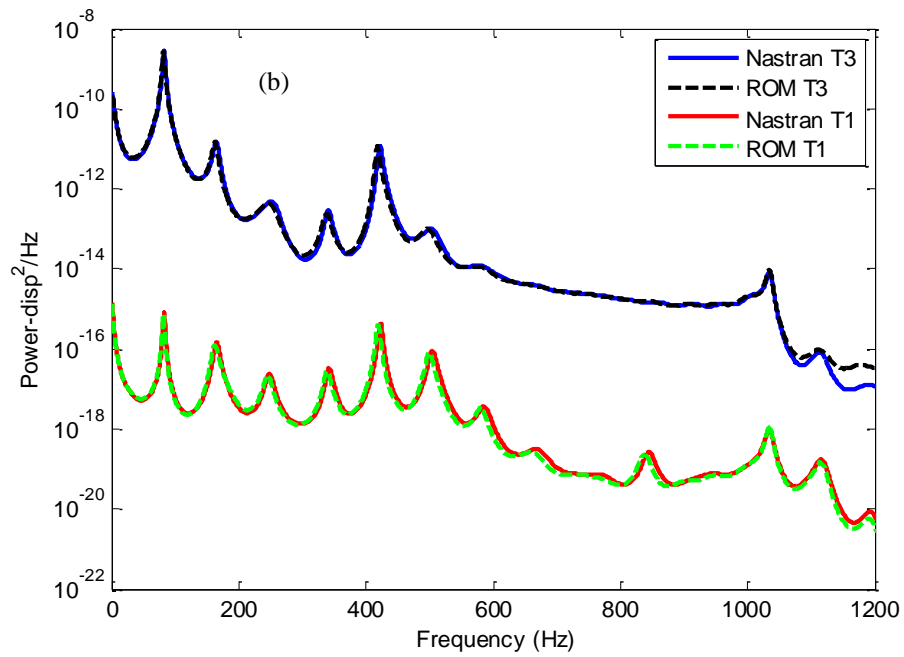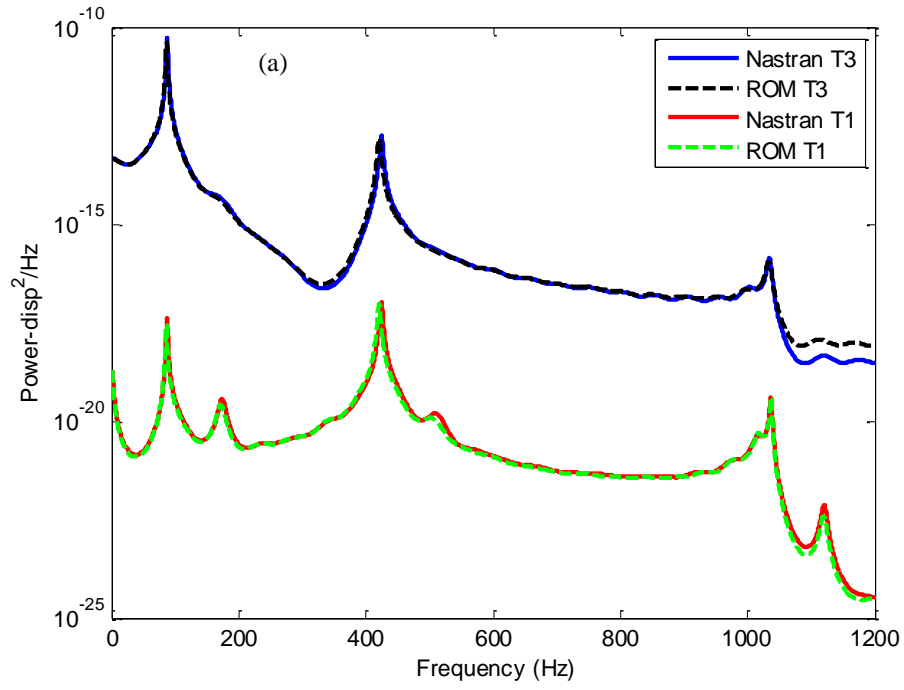
Figure 9. Power spectral density of the transverse (T3) and inplane (T1) deflections at the beam mid point. ROM and Nastran nonlinear predictions. Steady, offset heat flux and acoustic excitation of (a) *SPL* =110dB, (b) *SPL* =130dB, (c) *SPL* =145dB.
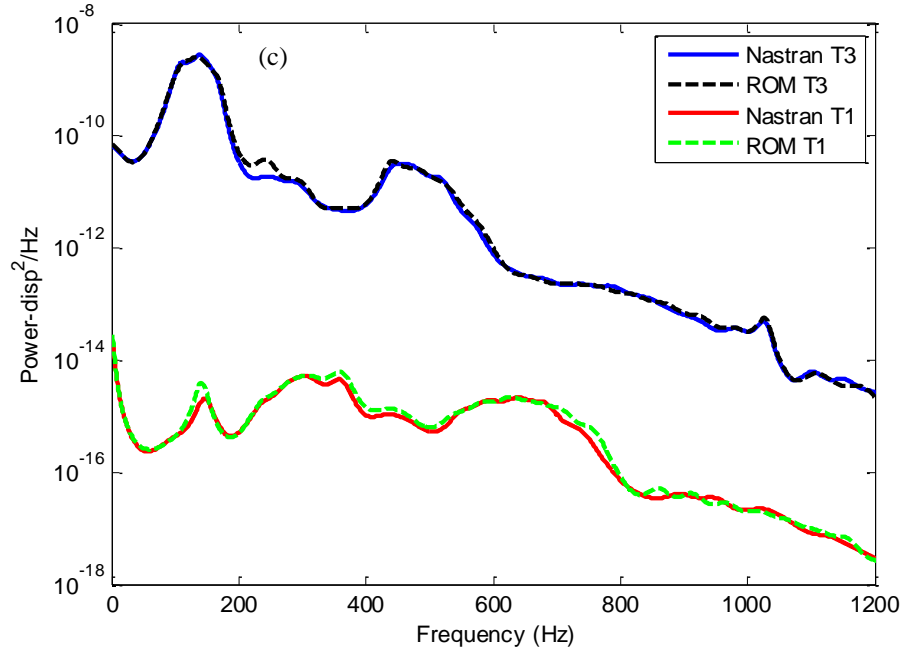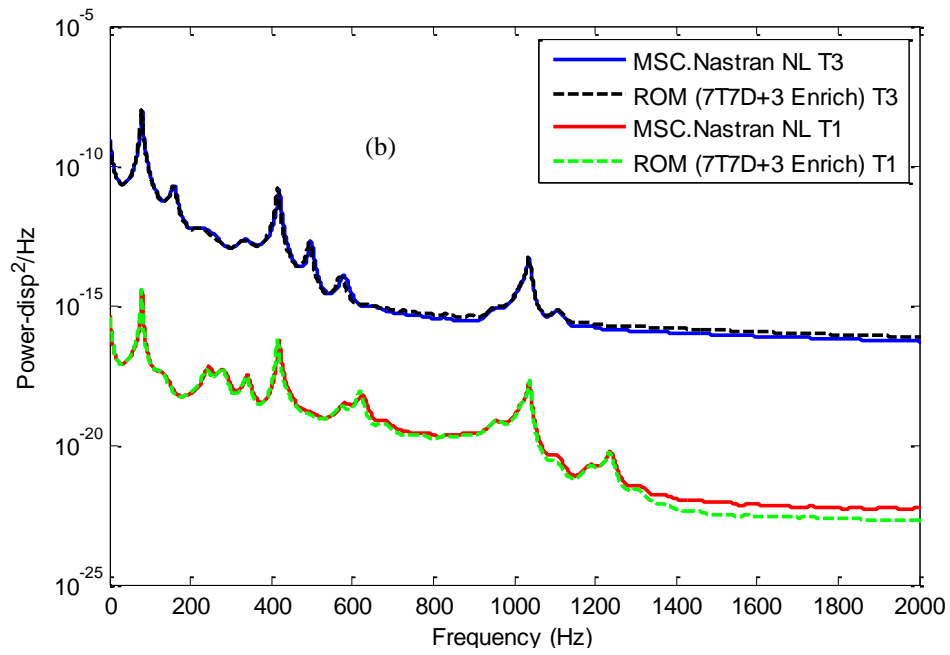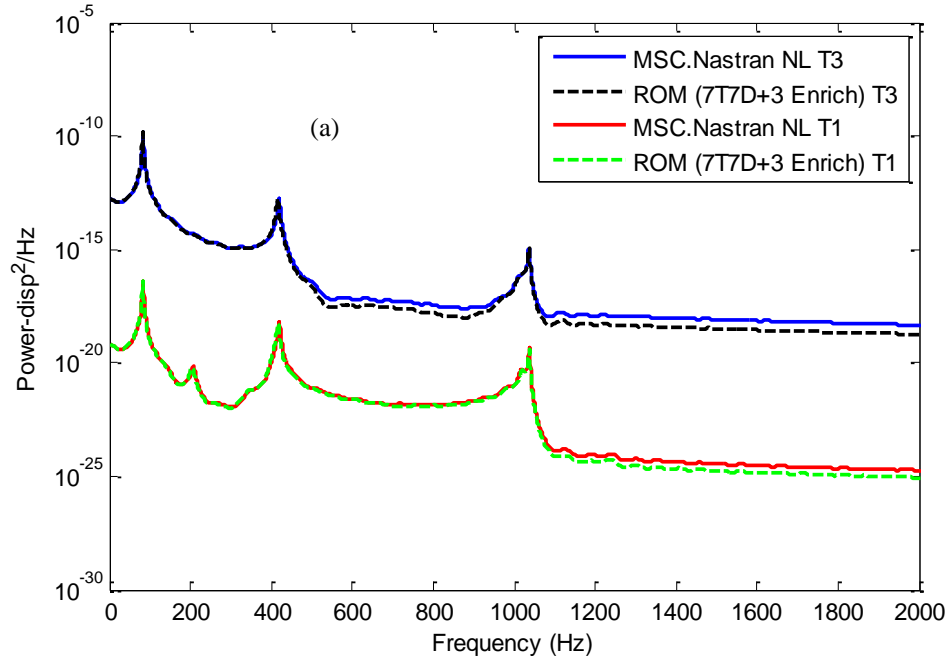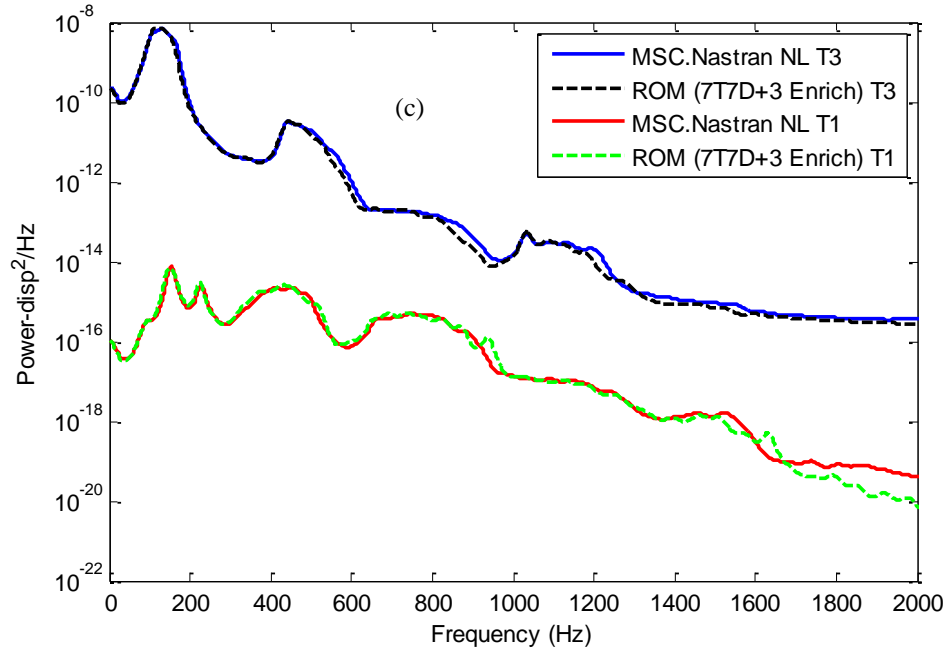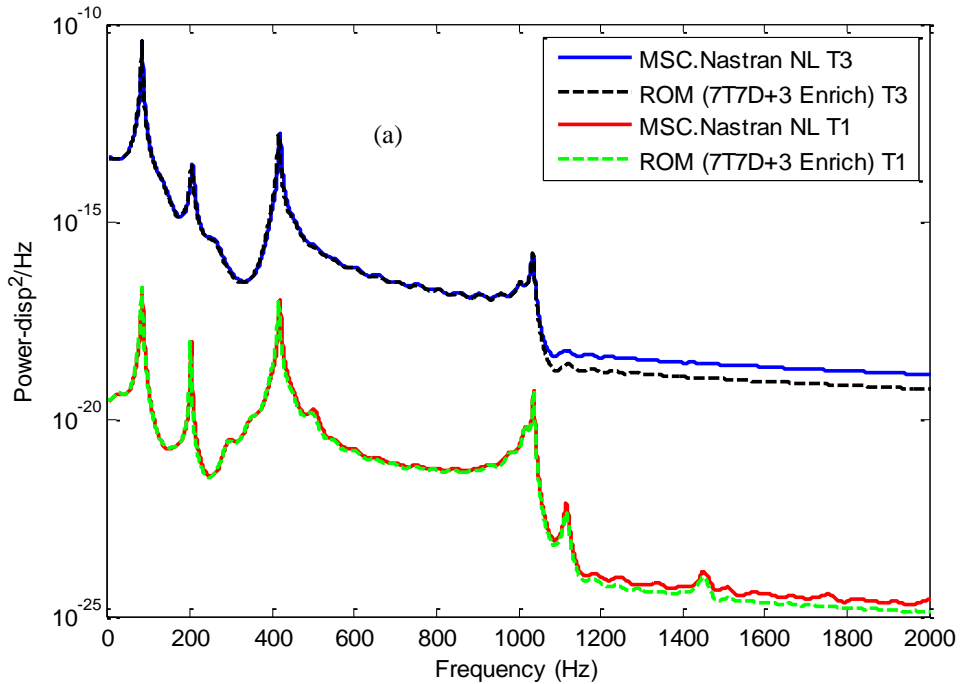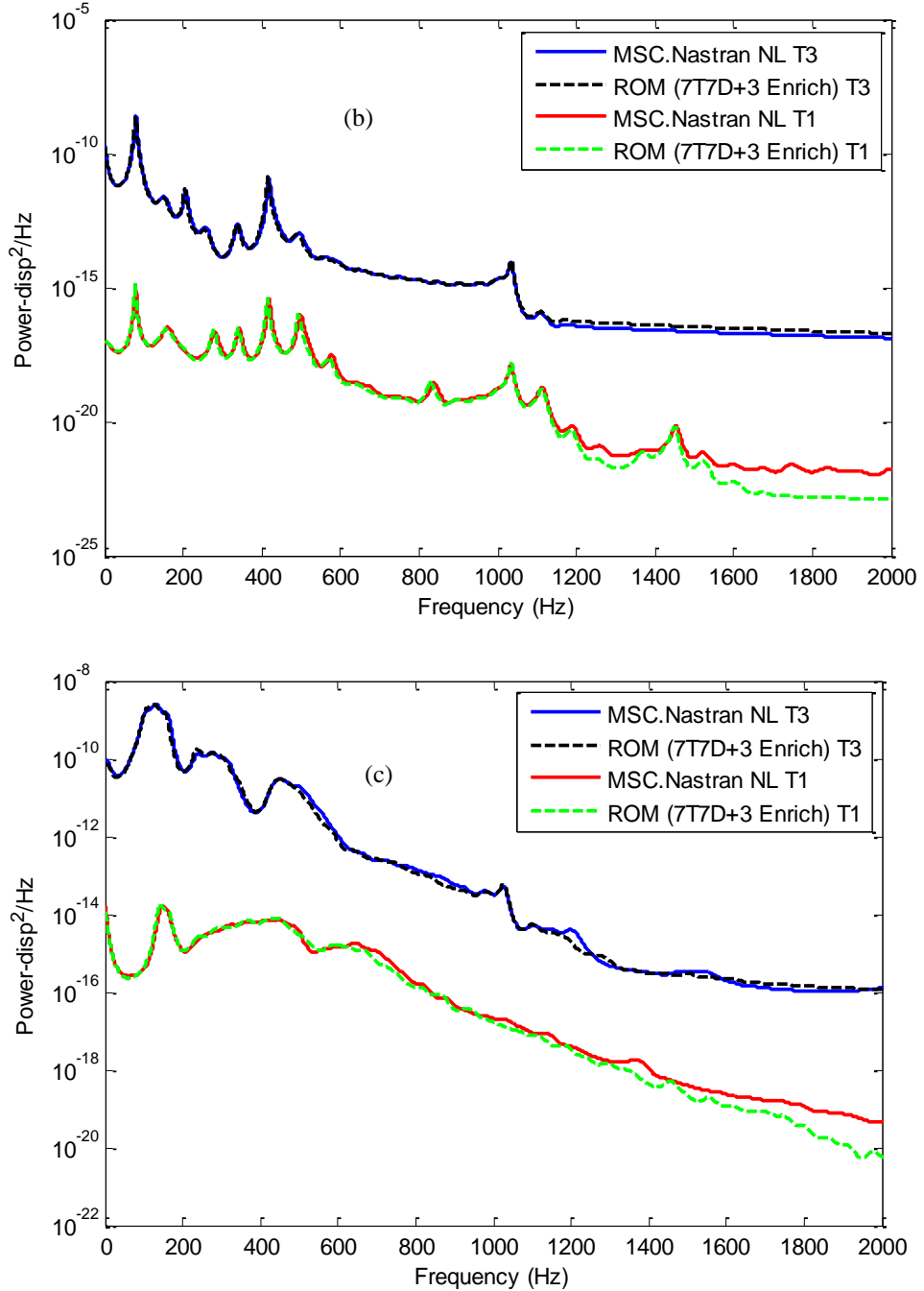
Figure 10. Power spectral density of the transverse (T3) and inplane (T1) deflections at the beam quarter point. ROM and Nastran nonlinear predictions. Steady, offset heat flux and acoustic excitation of (a) SPL =110dB, (b) SPL =130dB, (c) SPL =145dB.

CHAPTER 4 – OSCILLATING FLUX

4.1 Thermal Problem: Linear Through Thickness Temperature Distribution

Having validated the thermal and structural reduced order models to the steady heat flux case, it is now desired to proceed with the oscillation flux study. The amplitude of this oscillation, or δ (see Fig. 1), was selected as 7.5% of the beam length.

The first task in this effort is the determination of the steady state temperature field induced by the oscillating heat flux. In this regard, note that this flux is indeed periodic with period $2\pi/\Omega$ and thus can be represented as a Fourier series at every point of the top of the beam, i.e.

$$\underline{q}(t) = \underline{q}_0 + \sum_{n=1}^{\infty} \left[\underline{q}_n \cos n\Omega t + \hat{\underline{q}}_n \sin n\Omega t \right] \tag{61}$$

where the Fourier coefficients $\underline{q}_0$, $\underline{q}_n$, and $\hat{\underline{q}}_n$ can be evaluated by integration over a period length of the flux profile of Fig. 1 times sine and cosine functions of $n\Omega t$. Further, since the heat conduction equation is linear, it can be argued that the steady state temperatures at the entire set of grid points is of the form

$$\underline{T}(t) = \underline{T}_0 + \sum_{n=1}^{\infty} \left[\underline{T}_n \cos n\Omega t + \hat{\underline{T}}_n \sin n\Omega t \right]. \tag{62}$$

A similar representation of the thermal ROM generalized coordinates vector $\underline{\tau}(t)$ of components $\tau_j(t)$ can also be expected, i.e.

$$\underline{\tau}(t) = \underline{\tau}_0 + \sum_{n=1}^{\infty} \left[\underline{\tau}_n \cos n\Omega t + \hat{\underline{\tau}}_n \sin n\Omega t \right]. \tag{63}$$

36

The temperature vectors $\underline{T}_0$, $\underline{T}_n$, and $\underline{\hat{T}}_n$ can be obtained by introducing Eqs (61) and (62) in the heat conduction equation (in the finite element model)

$$B \frac{d\underline{T}}{dt} + K\underline{T} = \underline{q}(t) \tag{64}$$

which leads to the relations

$$K\underline{T}_0 = \underline{q}_0 \tag{65}$$

and

$$K\underline{T}_n + B(n\Omega)\underline{\hat{T}}_n = \underline{q}_n \tag{66}$$

$$-B(n\Omega)\underline{T}_n + K\underline{\hat{T}}_n = \underline{\hat{q}}_n \tag{67}$$

These relations permit the direct evaluation of $\underline{T}_0$, $\underline{T}_n$, and $\underline{\hat{T}}_n$, i.e. of the temperature representation, in terms of the flux specification.

A first approach to obtain the steady state representation of the thermal generalized coordinates $\tau_j(t)$ of Eq. (19) is thus to proceed with the solution of Eqs (64)-(67) and then project the distribution of Eq. (62) on Eq. (1) to obtain the coefficients of Eq. (64). An alternate approach is to apply a procedure similar to Eqs (65)-(67) to the thermal ROM governing equations, Eq. (19), to obtain the steady state representation of each of the temperature generalized coordinates $\tau_j(t)$, i.e. Eq. (63). The first approach was adopted in this thesis.

Shown in Fig. 11 is a comparison of the temperature distribution on top of the beam obtained through a time marching of the conduction problem in Nastran and the corresponding Fourier series approximation with 40 harmonics for a 1Hz oscillation of the flux ($\Omega = 2\pi$). Clearly, the agreement is excellent. To

37

complement this comparison, shown in Figs 12 and 13 are the time histories of the temperature at the middle of the beam and at a node near the furthest left excursion of the heat flux distribution for 1 and 80Hz oscillations. Again, the matching is excellent justifying the Fourier series representation.

Also shown on Figs 11-13 are the temperatures predicted by projecting the 40 harmonics series on the thermal basis. It is seen from these results that the matching is very good at the 1Hz oscillation frequency but degrades slightly as that frequency is increased to 80Hz. This finding suggests that the thermal basis should be increased somewhat as the frequency of the oscillations is increased. The effects of these differences on the structural response will be seen to be much reduced. Note finally that the variation of the temperature with time is significantly smaller at 80Hz than at 1Hz.

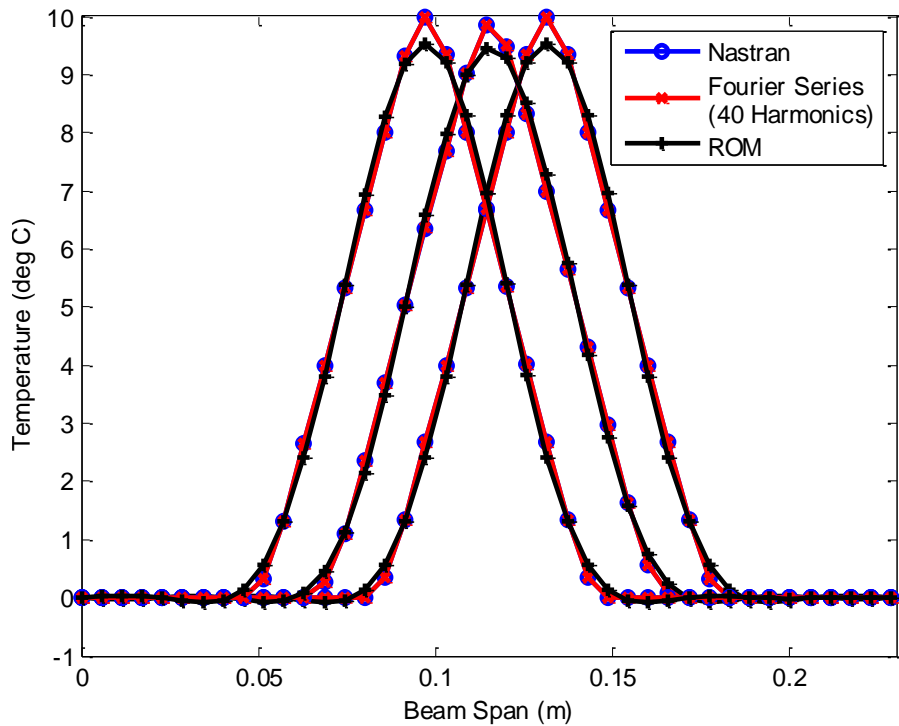Figure 11. Temperature distribution on the beam top surface;
oscillating heat flux, $\Omega = 2\pi(1Hz)$. Shown at the beginning,
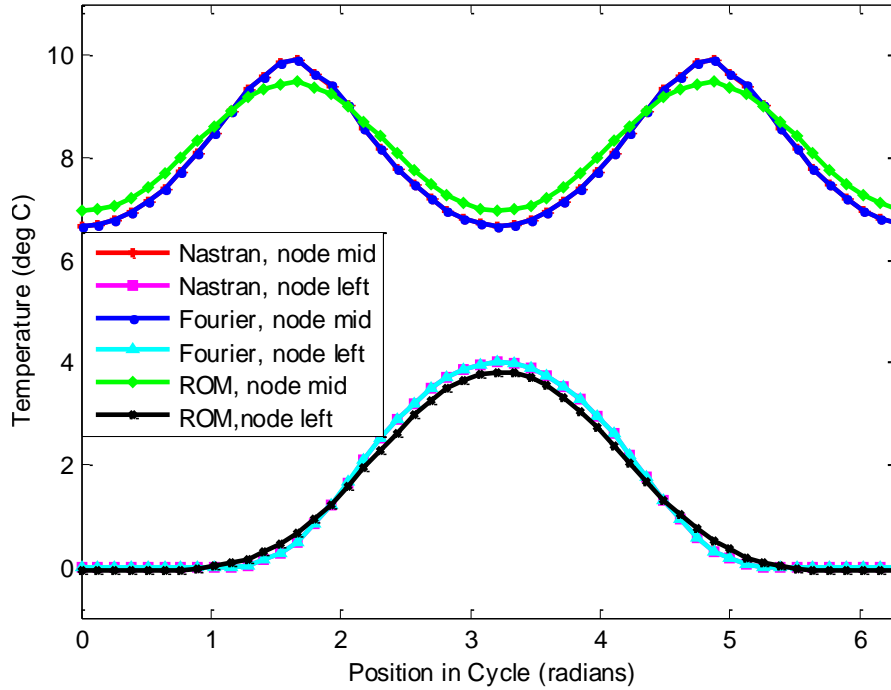quarter, and middle of the period. Nastran, Fourier series, and
ROM computations.

Figure 12. Time history of temperature at the beam middle and at a
node near the furthest left excursion of the flux, $\Omega = 2\pi (1Hz)$.
Nastran, Fourier series, and ROM computations.

Figure 13. Time history of temperature at the beam middle and at a
node near the furthest left excursion of the flux, $\Omega = 160\pi$ (80Hz).
Nastran, Fourier series, and ROM computations.

4.2 Structural Problem: Linear Through Thickness Temperature Distribution

A similar assessment of the structural reduced order model was considered

next before assessing the dependence of the response on the flux oscillation

frequency. To this end, shown in Figs 14-16 are comparisons of the transverse

and inplane deflections at beam middle and at a node near the furthest left

excursion of the heat flux obtained at oscillation frequencies of 1Hz, 40Hz, and

80Hz. Note that the nonlinear structural response was found to be periodic and

thus only 1 period is shown.

In Figs 14-16 and all ensuing ones, the Nastran responses shown were

obtained with a linear temperature through thickness (the only option allowed for

CBEAM elements), as opposed to the full temperature profile obtained in the

40

thermal computations. This linear distribution was obtained by retaining from the

full solution the temperature at the top and bottom surfaces of the panel. The

ROM temperature distribution was also linear through thickness per Eq. (45) but

represented a linear best fit of the nonlinear temperature profile. This dissimilarity

led to a slight difference in the temperature distribution of the Nastran and ROM

structural computations which is felt more significantly at higher oscillating

frequencies. To provide an additional basis for comparison, a best fit linear

through thickness temperature distribution was also imposed in the 80Hz response

Nastran computations, see Fig. 16. A slight but definite difference between both

Nastran results can be observed.

Figure 14. Time history of (a) transverse and (b) inplane deflections at the beam middle and at a node near the furthest left excursion of the flux, $\Omega = 2\pi(1\text{Hz})$. Nastran and ROM computations.
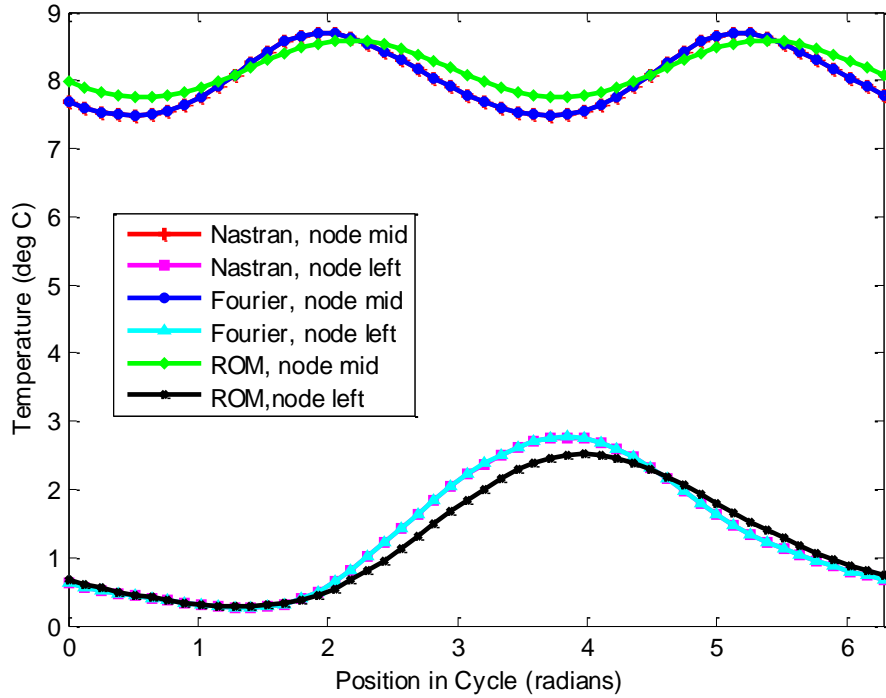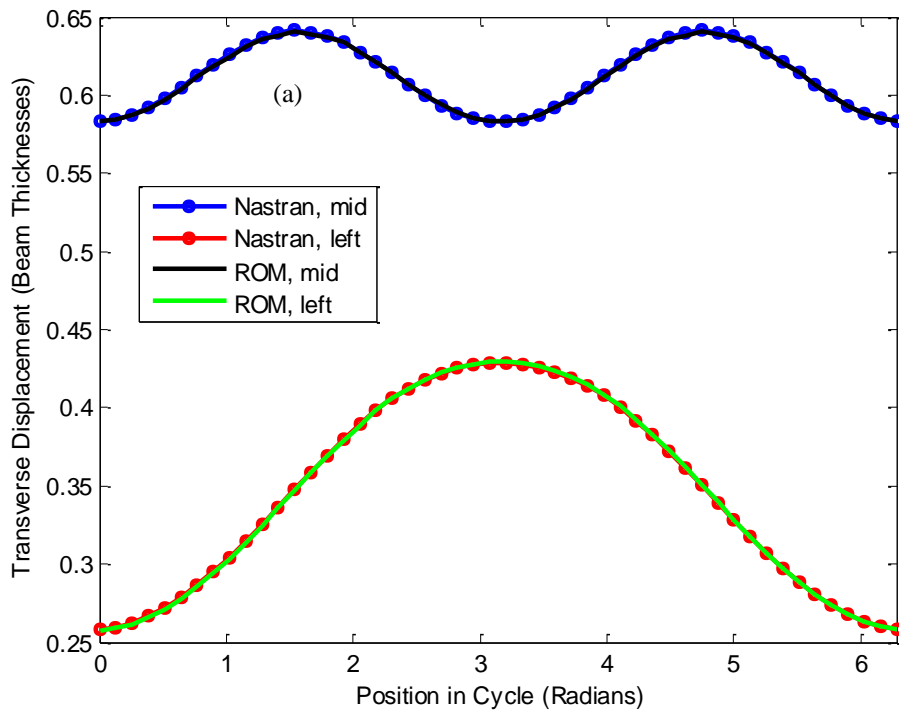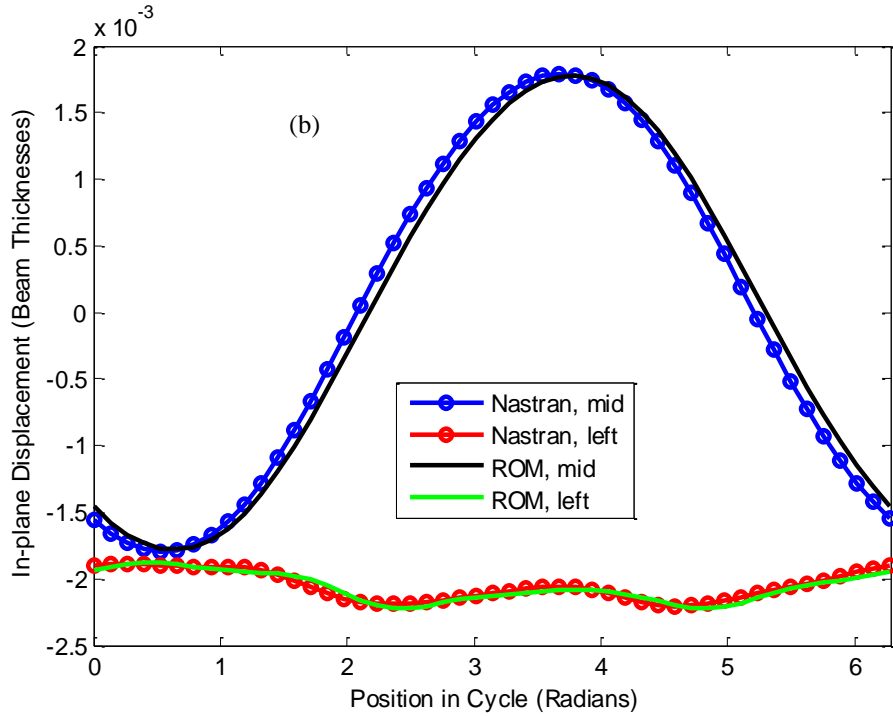
Figure 15. Time history of (a) transverse and (b) inplane deflections at the beam middle and at a node near the furthest left excursion of the flux, $\Omega = 80\pi$ (40Hz). Nastran and ROM computations.
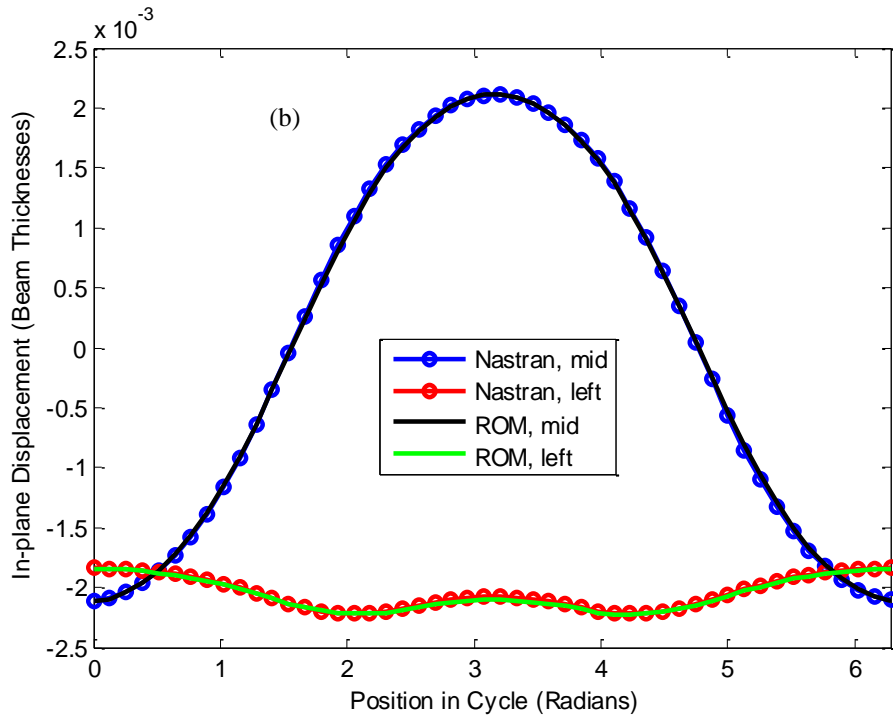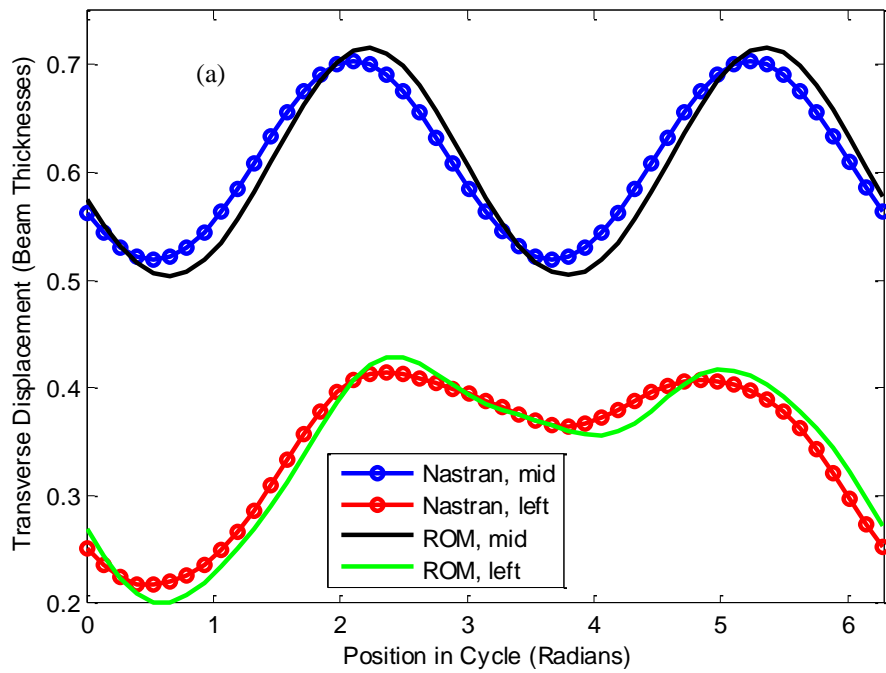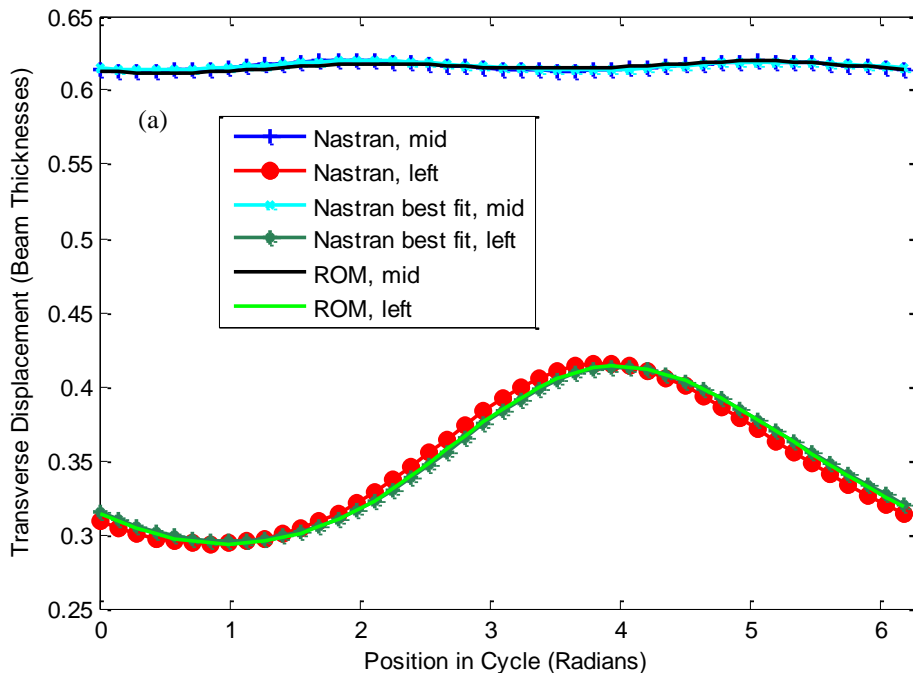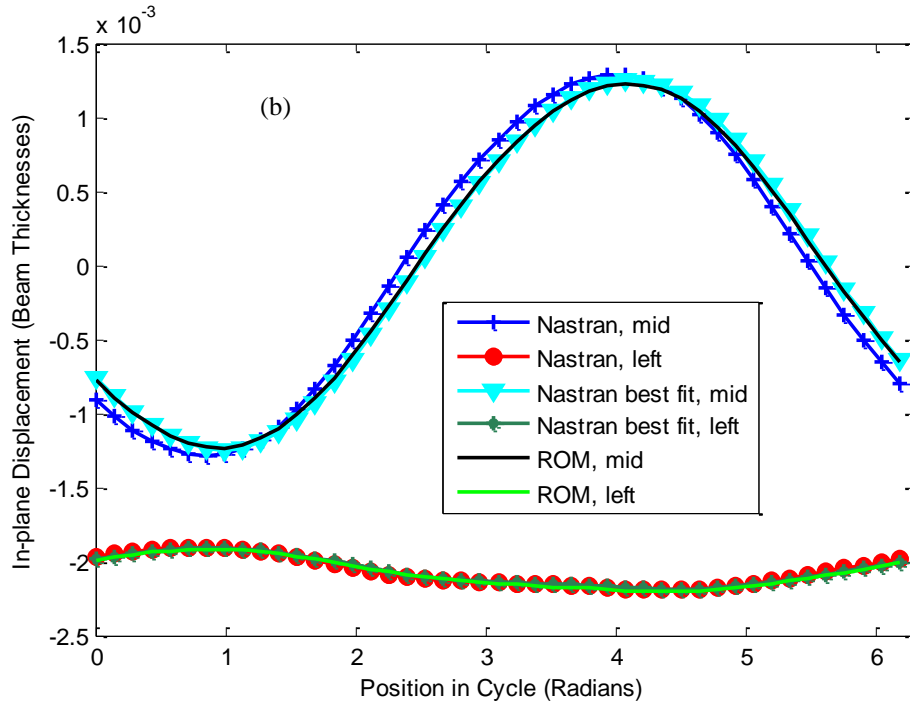
Figure 16. Time history of (a) transverse and (b) inplane
deflections at the beam middle and at a node near the furthest left
excursion of the flux, $\Omega = 160\pi(80\text{Hz})$. Nastran and ROM
computations. Also shown Nastran response with best fit linear
temperature.

Note from Figs 14-16 that the agreement of the Nastran and ROM
structural response is very good to excellent in all cases, even though slight
discrepancies in the temperature distributions between Nastran and ROM
occurred (see Figs 11-13). The largest discrepancy appears at 40Hz and
corresponds to a resonance condition (see discussion below). Note further, at the
80Hz oscillation frequency, the improved matching between the ROM
displacements and the Nastran computations carried out with the best fit linear
temperature. This finding suggests that discrepancies between the ROM and other
Nastran computations may be related to the treatment of the through thickness
nonlinearity of the temperature profile.

From Fig. 16, i.e. at the 80Hz flux oscillation frequency, a very small amplitude of the transverse motions at the middle of the beam is observed but much larger displacements occur at the left edge of the flux. The beam thus seems to vibrate in an antisymmetric manner around a near constant symmetric deformation.

It should further be observed that the dominant frequency in these time histories is not all the same. For example, the inplane motions exhibit a basic frequency of Ω while the transverse deflection of the middle point is periodic with frequency equal to 2Ω. The explanation of this behavior lies in the nature of the thermal and structural modes which are symmetric (both) for the odd numbered modes while the even ones are antisymmetric. Further, the coupling, both through the temperature dependent term of the linear stiffness matrix and the thermal moment term, occurs by even and odd pairs. That is, the symmetric structural modes are only directly excited through the symmetric thermal modes and vice versa. Note next that the symmetric thermal generalized variables will be identical when the flux reaches symmetric positions with respect to the middle, i.e. every 1/2 cycle. Thus, the symmetric part of the temperature distribution (and accordingly of the structural response) has a period twice of the heat flux as observed in Figs 14-16.

At a node near the furthest excursion of the heat flux, i.e. at $0.3*L$, the first antisymmetric mode is near its peak and thus affects strongly the response. Thus, the response there includes all harmonics of Ω at the contrary of the beam middle where only the even harmonics are observed. The above discussion would suggest

that the odd and even (symmetric and antisymmetric) motions are uncoupled in the present case. This is not so, as the symmetric transverse motions induce antisymmetric inplane displacements and thus a nonlinear coupling does exist.

4.2.1 Parametric Study of Oscillation Frequency

The above discussion holds in the particular case selected here of a heat flux oscillating around the middle of the beam, i.e. $a_0 = L/2$. In the more general case, all responses would exhibit components of frequencies $n\Omega$, $n = 1, 2, ...,$ of varying magnitudes. Then, the prototypical governing equation for a particular structural generalized coordinate would be

$$
\begin{aligned}
\ddot{q} + c\dot{q} + \left(K^{(1)} - K_{th}^{(1)} \tau_0 \sin n\Omega t \right) q + K^{(2)} q^{(2)} \\
+ K^{(3)} q^3 = F_0(t) + F^{(th)} \tau_0 \sin n\Omega t
\end{aligned}
\tag{68}
$$

assuming that the dominant thermal generalized coordinate τ exhibits a frequency $n\Omega$, i.e. $\tau(t) = \tau_0 \sin n\Omega t$. Equation (68) is a nonlinear Mathieu equation externally excited by the second term on the right-hand-side. Then, relying on classical analyses (e.g. see [23]) it is expected that resonances would occur in the linear case at the frequencies $\sqrt{K^{(1)}} = (m/2)n\Omega$ where $m = 1, 2, ...$ with, in particular, $m = 1$ being the primary resonance for the parametric excitation and $m = 2$ leading to resonance with the right-hand-side term.

To clarify the possibility of resonances in the case considered here, the 17-mode structural 10-mode thermal reduced order model was used with oscillating flux frequency in the range of 16-110Hz which would provide several possible

resonances with the dominant transverse mode of linear frequency equal to 79.6Hz. For each oscillation frequency Ω, the Fourier coefficients (40 harmonics) of the temperature distribution were obtained and projected on the thermal ROM to obtain the steady state time evolution of the thermal generalized coordinates. Then, the structural ROM was marched in time with these coordinates until a periodic solution was reached, which occurred in all cases observed. Then, the peak transverse displacement on the beam was recorded.

The results of this parametric study are presented in Fig. 17 which shows the largest response on the beam and at the middle as a function of the oscillation frequency Ω.
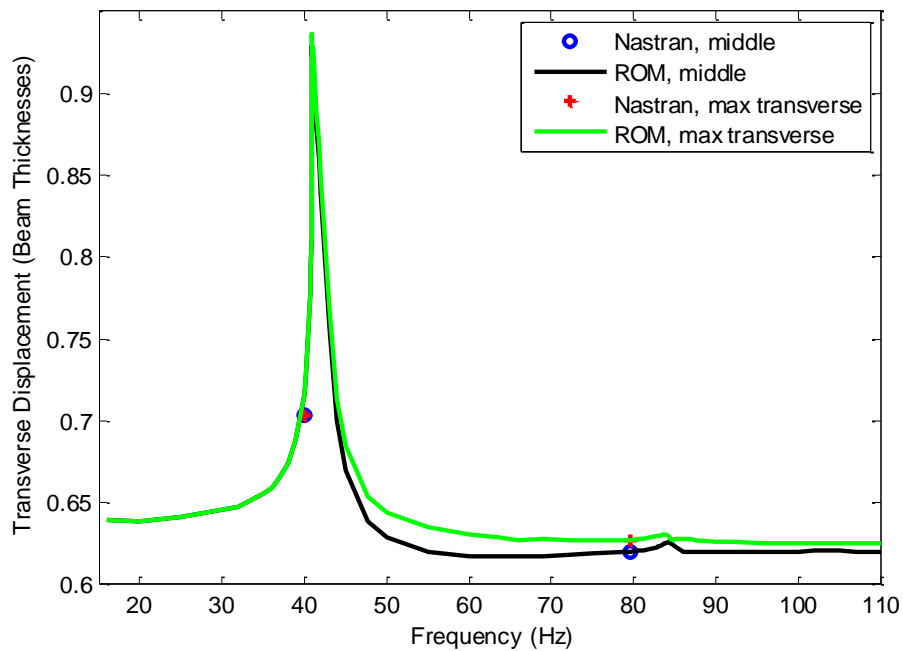

Figure 17. Maximum transverse deflection achieved on the beam and at the beam middle as a function of the flux oscillation frequency Ω as determined from the ROM and Nastran computations.

47

It is seen that the largest response occurs near 41Hz and corresponds to $n = 2$ (since the first mode is excited at twice the oscillation frequency, see discussion above) and $m = 2$, i.e. for the resonance induced by the right-hand-side term. A much smaller peak also occurs near 80Hz which could be associated with the primary parametric resonance ($m = 1$, $n = 2$) or with resonance with the right-hand-side term induced by the first harmonic ($m = 2$, $n = 1$) or a combination of both effects. Note further that the peak of the response occurs at the middle of the beam for frequencies below the resonance (40.9Hz) but is achieved very close from that midpoint for frequencies above 40.9Hz. This finding suggests a slight compounding effect of the antisymmetric modes, see above discussion of Fig. 16(a).

4.2.2 Validation With Acoustic Loading

The next component of the current investigation focused on the response of the beam to the combined oscillating flux and acoustic excitation. In this context, shown in Figs 18 and 19 are the spectra of the transverse and inplane displacements at the beam middle and quarter points, obtained at an oscillation frequency of 20Hz and a sound pressure level of 130dB. A comparison of these results with those obtained in the steady flux case, see Figs 7 through 10, demonstrates that the structural response is modified primarily in the low frequency part and most notably inplane as opposed to transverse.
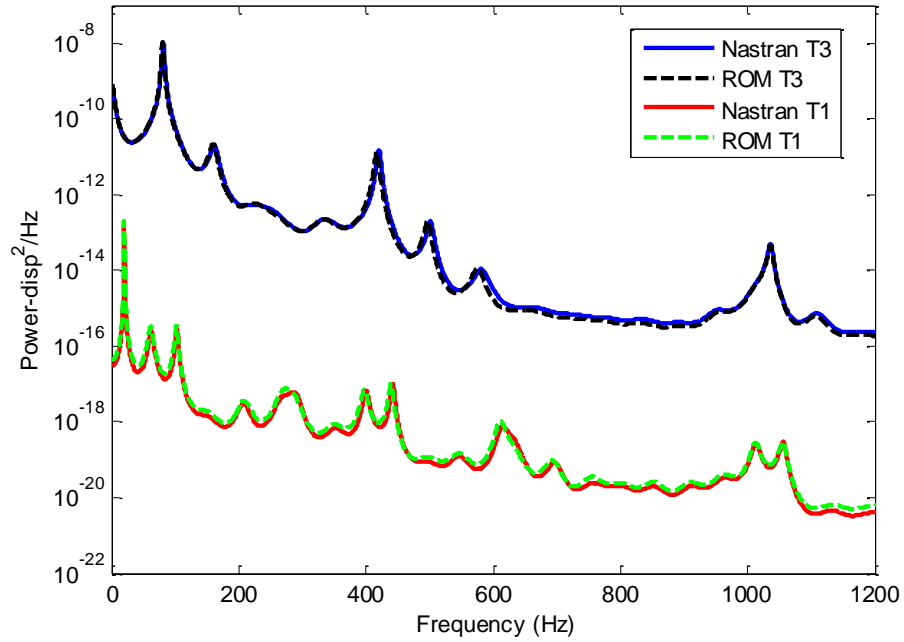
Figure 18. Power spectral density of the transverse (T3) and inplane (T1) deflections at the beam middle. ROM and Nastran nonlinear predictions. Oscillating heat flux, $\Omega=40\pi$ (20Hz), and acoustic excitation of *SPL* =130dB.

Figure 19. Power spectral density of the transverse (T3) and inplane (T1) deflections at the beam quarter point. ROM and

Nastran nonlinear. Oscillating heat flux, Ω=40π (20Hz), and acoustic excitation of *SPL* =130dB.

The above computations were also repeated at 40Hz near the 40.9Hz resonance, see Figs 20 and 21. A comparison of Figs 18-19 and 20-21 confirms that the largest differences are indeed observed in the inplane displacements and most specifically in the low frequency range, although the magnitude of the 200Hz peak in the transverse spectrum is significantly higher in the 40Hz case.

Figure 20. Power spectral density of the transverse (T3) and inplane (T1) deflections at the beam middle. ROM and Nastran nonlinear. Oscillating heat flux, Ω=80π (40Hz), and acoustic excitation of *SPL* =130dB.
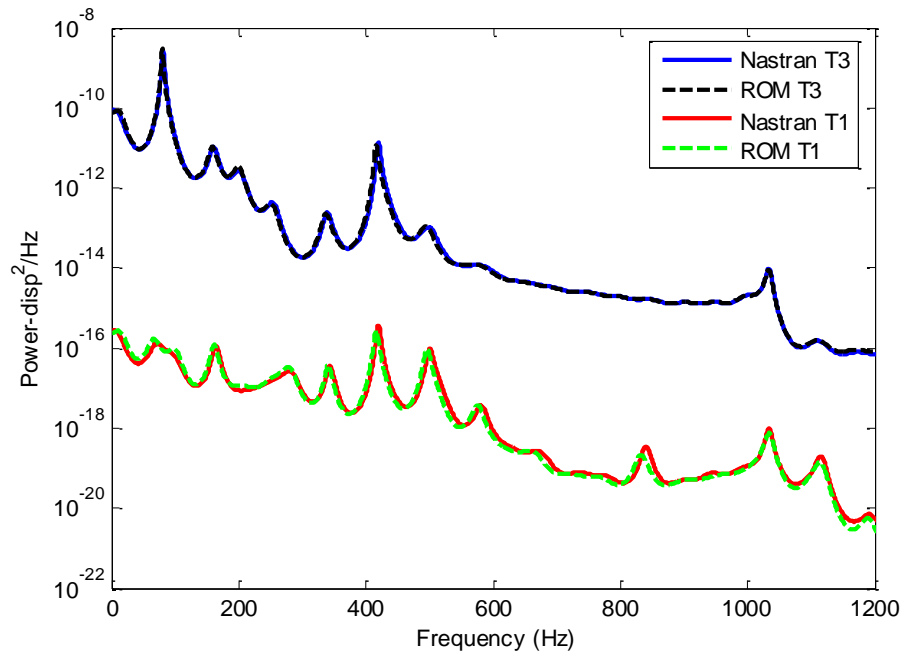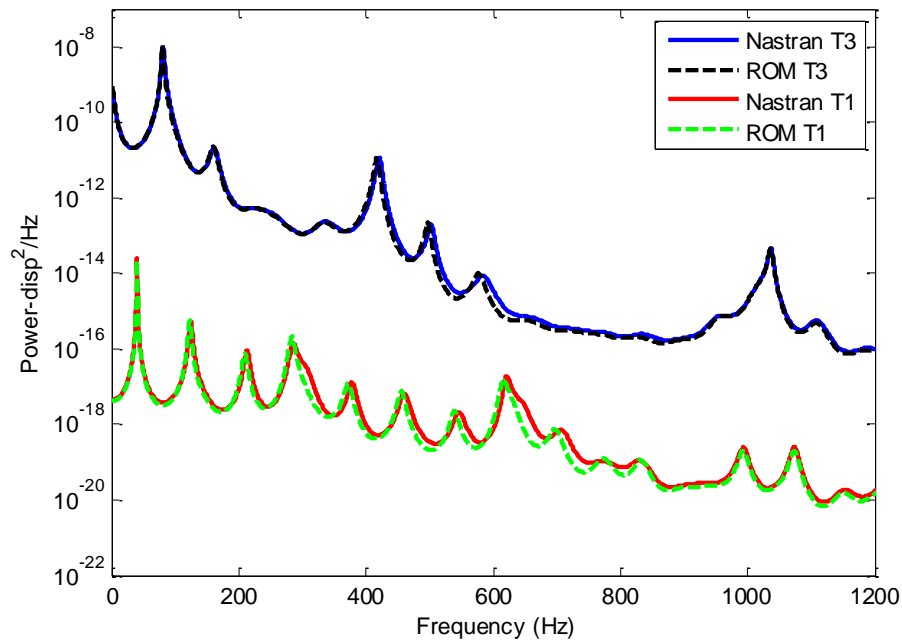
Figure 21. Power spectral density of the transverse (T3) and inplane (T1) deflections at the beam quarter point. ROM and Nastran nonlinear. Oscillating heat flux, $\Omega=80\pi$ (40Hz), and acoustic excitation of *SPL* =130dB.

4.3 Improved Validation Efforts

The comparison of Nastran results of Fig. 16 obtained with two different linear approximations of the through thickness temperature distribution suggest that the nonlinearity of this distribution affects the structural response. It was accordingly desired to improve the thermal reduced order modeling to capture this nonlinearity and the effects it has on the structural response.

4.3.1 Thermal Problem: Linear and Cubic Through Thickness Distribution

In order to improve the thermal basis, the linear through thickness modes were combined with both quadratic and cubic through thickness modes and were tested in order to see which would be most beneficial to include. Figures 22 and

51

23 show the capturing of the true through thickness temperature profile for an oscillating frequency of 80 Hz by linear, linear with quadratic, and linear with cubic through thickness modes at particular locations along the beam and times in the cycle. Specifically, Fig. 22 shows the through thickness temperature profile near the furthest right edge of the heat flux when the heat flux is positioned at its furthest right point. Figure 23 similarly shows the through thickness temperature profile but near the furthest left edge of the heat flux when the heat flux is positioned at the beam center. In both of these plots, it is seen that the linear approximation of the through thickness temperature distribution is not good but that the inclusion of a cubic through thickness dependence leads to a close fit of the finite element results, better so than a quadratic term.
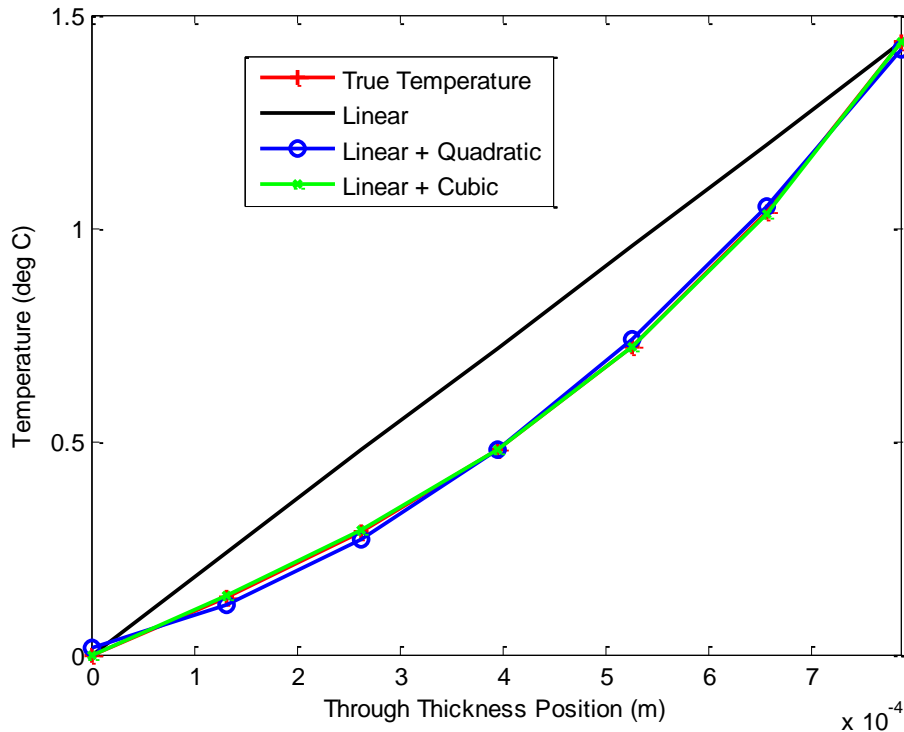

Figure 22. Linear, quadratic and cubic through thickness modes capturing the true temperature near the right edge of the heat flux when the heat flux is at its furthest right position.

52
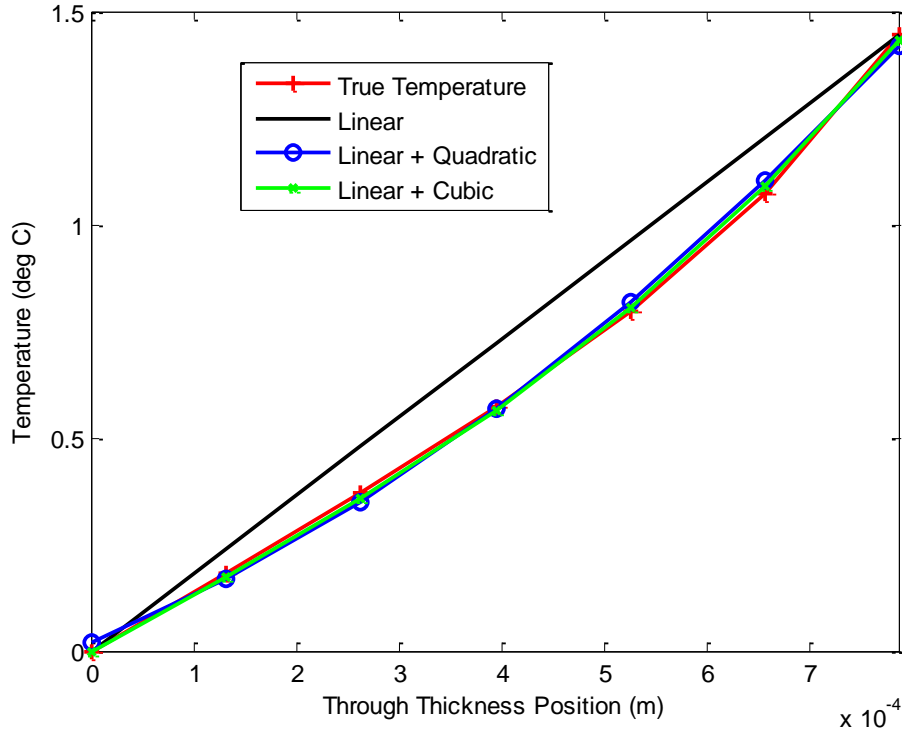
Figure 23. Linear, quadratic and cubic through thickness modes capturing the true temperature near the left edge of the heat flux as the heat flux is passing over the center of the beam.

The eigenvectors of the capacitance-conductance generalized eigenvalue problem associated with the 1-D heat conduction problem on the top surface of the beam, i.e. $T_{p,eig}^{(m)}\left(\underline{X}_p\right)$, were multiplied by the linear and cubic through thickness functions in order to form potential basis vectors. It was decided that the first eight eigenvectors with linear through thickness properties and the first eight eigenvectors with cubic through thickness properties would be selected as the thermal basis. Additionally, the 13th and 15th eigenvectors with linear through thickness properties were also selected, as these enabled the model to better capture the peak temperatures. Figures 24 and 25 show this 18 mode thermal model capturing the temperature profile on the top of the beam when the heat

source is oscillating at 1 Hz and 80 Hz, respectively. The matching is significantly improved over the 10 mode thermal model results of Figs 12 and 13. In regards to this assessment, it should be noted that the results of Figs 12 and 13 were obtained with a projection of the temperature field onto the thermal ROM basis, while Figs 24 and 25 represent the full thermal ROM, i.e. the generalized coordinates were found from a time marching of Eq. (19), without structural deformations, until steady state was reached.
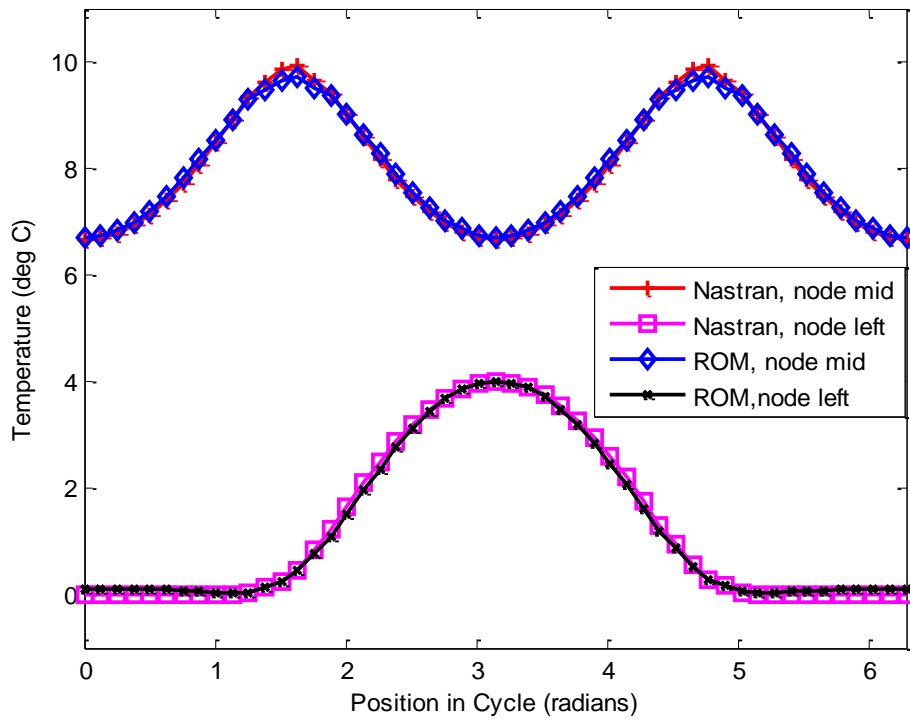

Figure 24. Time history of temperature at the beam middle and at a node near the furthest left excursion of the flux, $\Omega = 2\pi$ (1Hz). Nastran, and 18 mode thermal ROM computations.

Figure 25. Time history of temperature at the beam middle and at a
node near the furthest left excursion of the flux, $\Omega = 160\pi$ (80Hz).
Nastran, and 18 mode thermal ROM computations.

4.3.2 Structural Problem: ROM and Nastran Using Equal Temperature Loading

The results of Fig. 16 have demonstrated that the structural response may

be sensitive to the presence of nonlinearity in the through thickness temperature

distribution. Further, the matching of the reduced order model predictions were

found to be improved when using a best linear fit temperature in Nastran vs. the

linear distribution dictated by the temperature on top. It would be highly desirable

to perform a comparison of the structural responses predicted from the combined

thermal-structural ROM with linear+cubic temperature distribution through

thickness and from Nastran with the Nastran predicted, nonlinear through

thickness temperature distribution.

Unfortunately, this Nastran computation is not possible within the structural model adopted as the CBEAM element only supports a linear temperature distribution. Thus, the best possible validation of the structural ROM with Nastran is on a common linear through thickness temperature distribution. Figure 16 falls slightly short of providing this comparison as the best fit linear temperature does not exactly match the one used in the 10 mode thermal ROM.

To perform the desired comparison, the Nastran computations were repeated once more with the linear temperature distribution predicted from the thermal ROM. Then, shown in Figs 26-27 are comparisons of the transverse and inplane deflections at beam middle and at a node near the furthest left excursion of the heat flux obtained at oscillation frequencies of 40Hz and 80Hz. The results have improved significantly from Figs 15-16, although the most significant differences still occur near resonant frequencies.

Figure 26. Time history of (a) transverse and (b) inplane
deflections at the beam middle and at a node near the furthest left
excursion of the flux, $\Omega = 80\pi$ (40Hz). Nastran and ROM
computations.

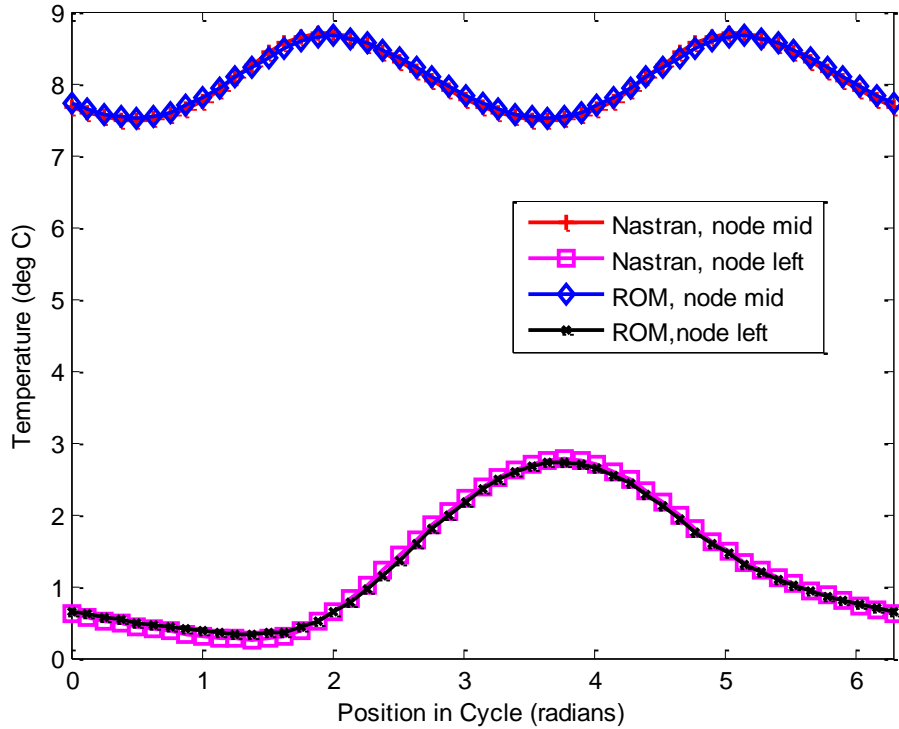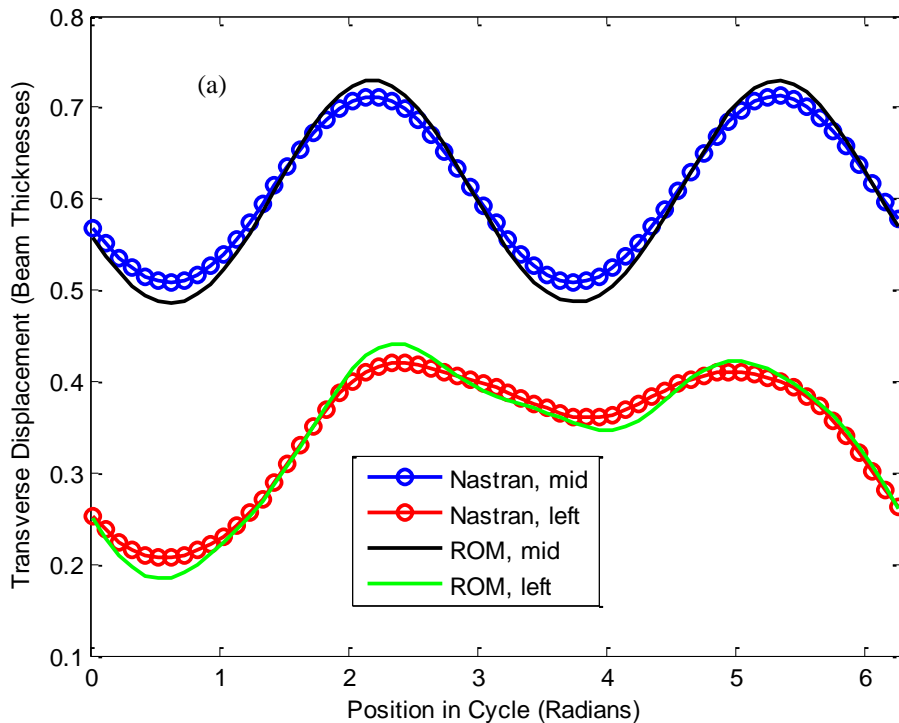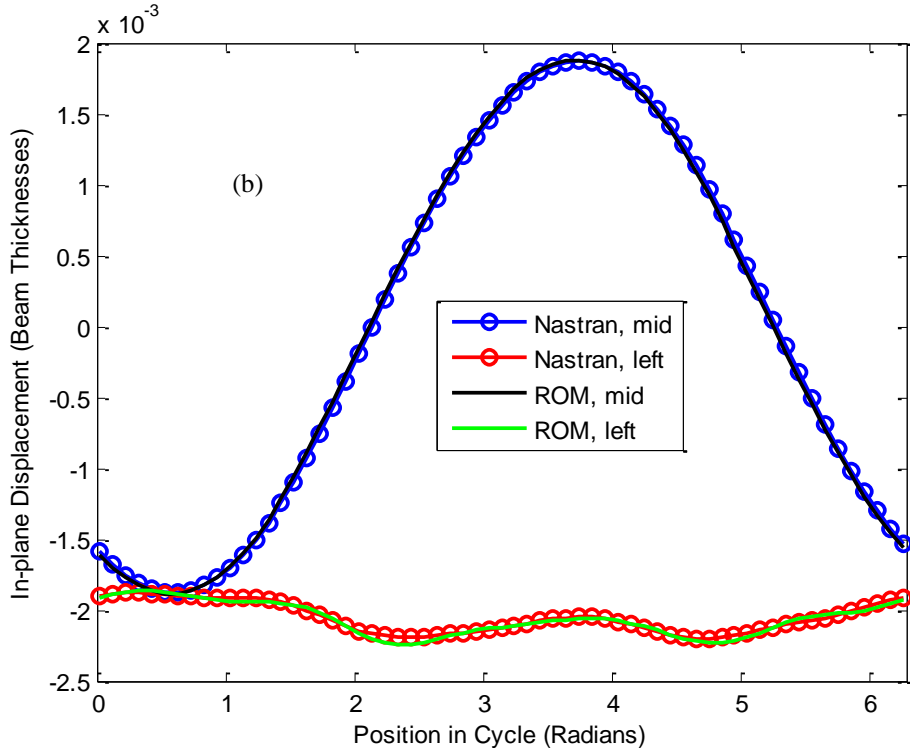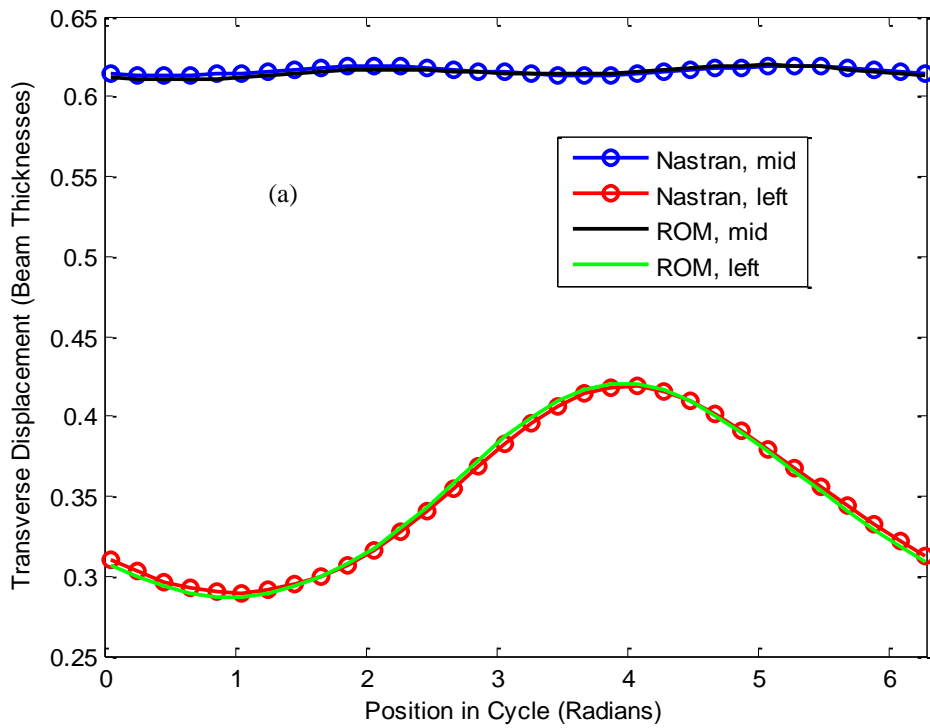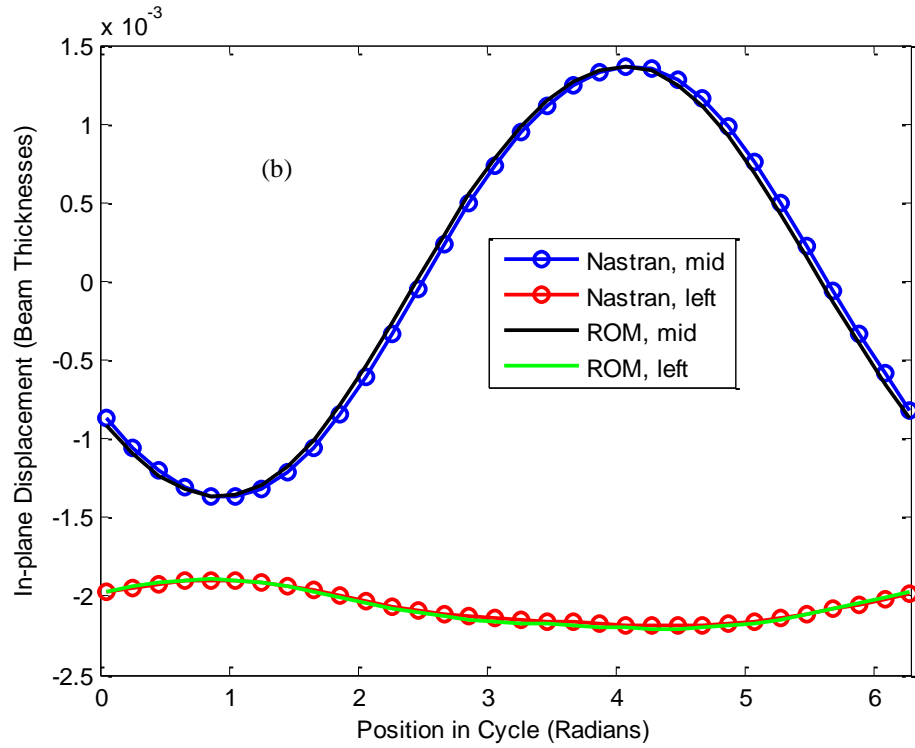Figure 27. Time history of (a) transverse and (b) inplane deflections at the beam middle and at a node near the furthest left excursion of the flux, $\Omega = 160\pi(80\text{Hz})$. Nastran and ROM computations.

CHAPTER 5 –TEMPERATURE DEPENDENT STRUCTURAL PROPERTIES

ROM VALIDATION

The final focus of this thesis was on performing a first validation of the

reduced order modeling with temperature dependent material properties. The

beam of properties specified by Table 1 at zero temperature was considered again

for reduced order modeling and validation with full Nastran computations. In

keeping with the first validation of the methodology, the temperature on the beam

was assumed to be constant throughout. For such a situation, only 1 thermal mode

is necessary and the structural ROM of [16] with 4 transverse modes, 4 dual

modes is appropriate.

To validate the model, it was first desired (case 1) that the coefficients of

thermal expansion α alone change with temperature, with E held constant (as

well as the Poisson's ratio ν since this parameter appears to vary only very little

with temperature). In the second case, the Young's modulus E was allowed to

vary with temperature while α was held constant, and, finally (case 3), both

properties were set to change with temperature. Since the purpose of this

investigation was to validate the reduced order modeling approach, the values of

the linear coefficients $\alpha^{(1)}$ and $E^{(1)}$ of

$$E = E^{(0)} - E^{(1)} T \tag{69}$$

and

$$\alpha = \alpha^{(0)} - \alpha^{(1)} T \tag{70}$$

were selected to observe changes in the structural response, not to model a

particular material, see Table 2 for specific properties for each of the 3 cases.

Table 2. Temperature Dependent Properties Specified

Case	$E^{(0)}$ (Pa)	$E^{(1)}$ (Pa/°C)	$\alpha^{(0)}$ (1/°C)	$\alpha^{(1)}$ (1/°C)^2
1	7.3 10^{10}	0.0	2.5 10^{-5}	5.0 10^{-7}
2	7.3 10^{10}	3.0 10^{8}	2.5 10^{-5}	0.0
3	7.3 10^{10}	3.0 10^{8}	2.5 10^{-5}	5.0 10^{-7}

In all cases a uniform temperature of 10 degrees Celsius was applied to the beam.

Figure 28 shows the transverse and inplane response for the first case and for both

temperature dependent (labeled "temp") and temperature independent models.

The reduced order model matches very well the Nastran predictions.
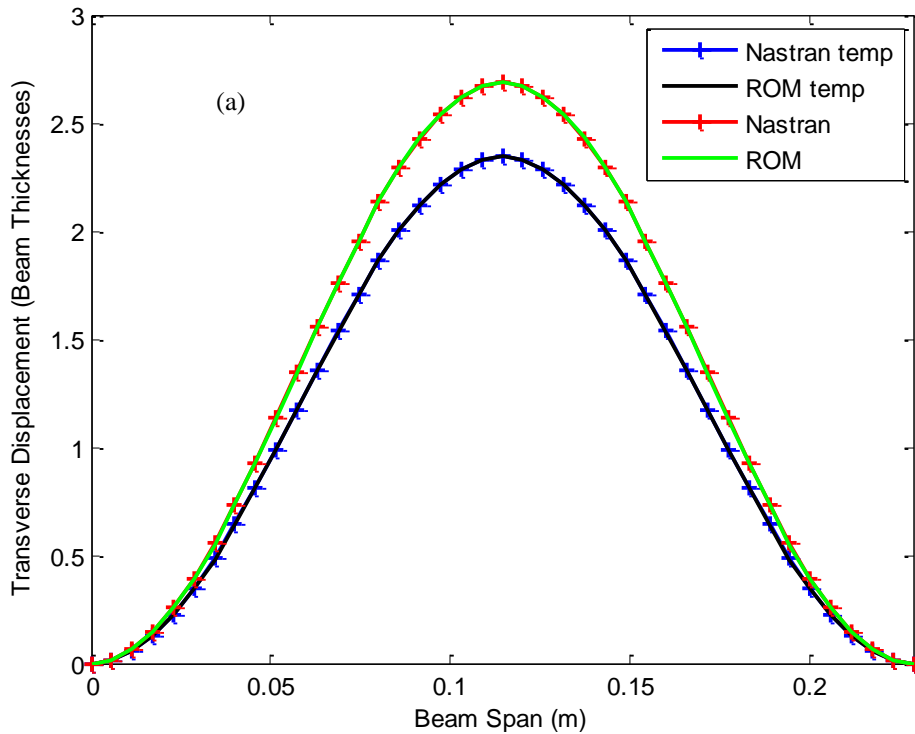
Figure 28. Displacements, (a) transverse, (b) inplane, for Case 1
induced by the uniform temperature field. ROM and Nastran
results for both temperature dependent and independent properties.

The corresponding results for the second case, in which the Young's modulus
changes with temperature but not the coefficient of thermal expansion, are shown
in Fig. 29. Note in fact that there is no difference in the structural response as
compared to the temperature independent beam. This finding is indeed expected
because the beam considered is homogenous and the temperature is constant
throughout. Thus, all stiffness coefficients (linear, quadratic, and cubic) and the
thermal moment terms are all proportional to the Young's modulus at 10°C which
then cancels out from both sides of Eq. (18) leaving the response to be
independent of the Young's modulus.

In the final case, both Young's modulus and coefficient of thermal
expansion were selected to be temperature dependent. The corresponding

61

comparison of responses predicted by the ROM with those obtained from Nastran is again excellent.

The excellent matching between Nastran and ROM results obtained in all 3 cases provides the desired first validation of the reduced order modeling procedure with temperature dependent properties.
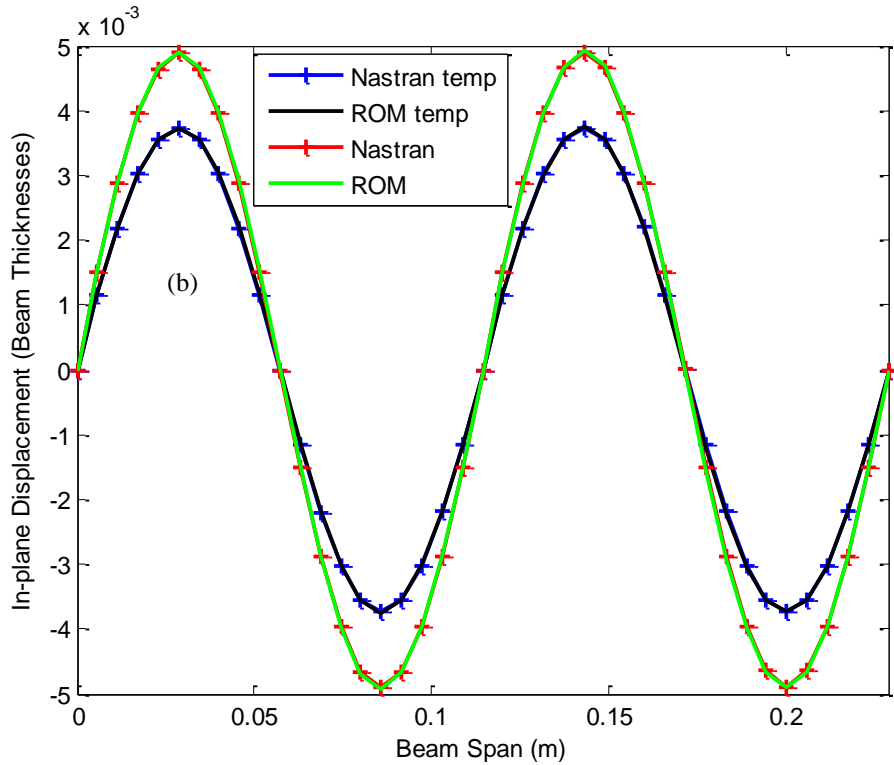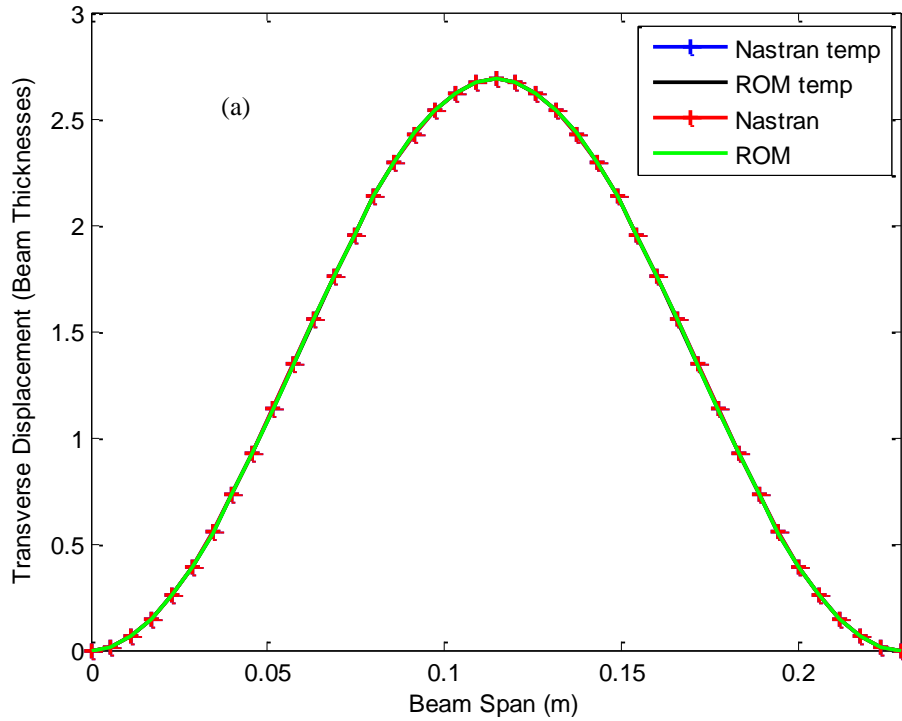
Figure 29. Displacements, (a) transverse, (b) inplane, for Case 2 induced by the uniform temperature field. ROM and Nastran results for both temperature dependent and independent properties.
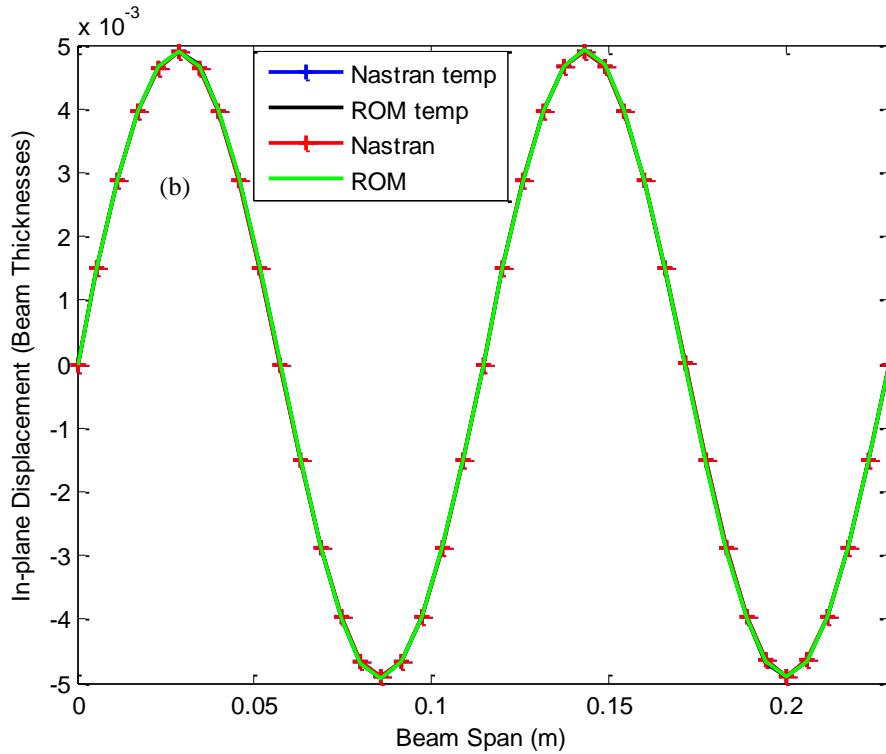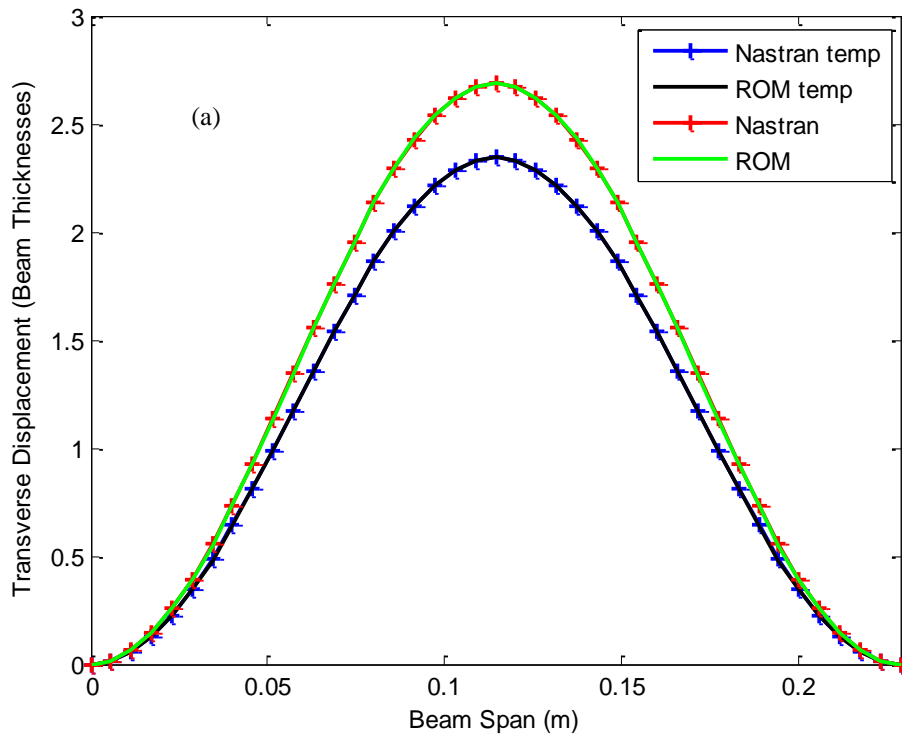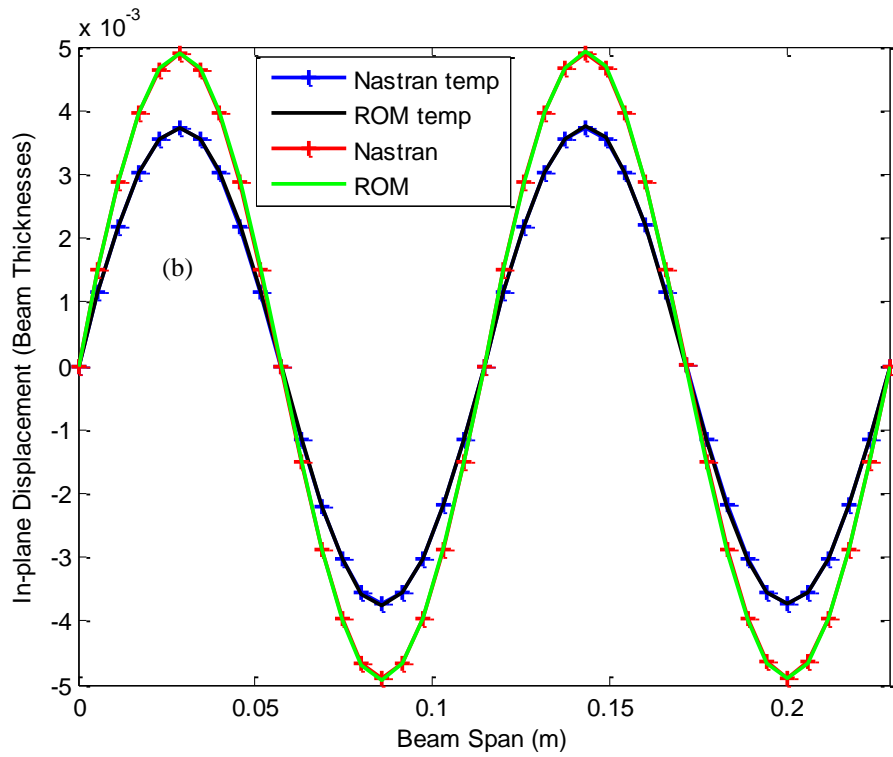
Figure 30. Displacements, (a) transverse, (b) inplane, for Case 3
induced by the uniform temperature field. ROM and Nastran
results for both temperature dependent and independent properties.

CHAPTER 6 – SUMMARY

The focus of this investigation was on the continued validation, application, and extension of thermal-structural reduced order modeling for nonlinear geometric structures subjected to thermal and mechanical loads.

First investigated was the unsteady temperature distribution and structural response induced by an oscillating flux on the top surface of a flat panel as a simple model of the thermal effects induced by an oscillating shock. This problem represents also an excellent platform for the continued validation of a combined structural-thermal reduced order modeling technique recently proposed.

In this regard, it was observed that a 10-mode thermal and 17-mode structural model led to structural responses and temperature distributions on the panel surface that match well to very well those obtained with full Nastran computations. Nevertheless, the through thickness temperature distribution was found to exhibit a definite nonlinearity not captured by the 10-mode thermal ROM basis but well represented by an extended, 18-mode basis including not only linear but also cubic dependence of the through thickness coordinate z.

A parametric study of the effects of the oscillation frequency of the heat flux has demonstrated the potential existence of multiple resonances with only one notably observed in the present investigation. These resonances arise first from the near coincidence of a linear natural frequency with a harmonic of the oscillating flux frequency. However, it was recognized that the temperature variations also affect the linear stiffness properties of the structural reduced order model leading to possible Mathieu-like parametric resonances which were not

65

found to be significant in the example considered. An increase by 50% of the peak structural response was observed at the sharp resonance occurring at half of the first natural frequency of the panel.

Finally, the combined effects of an oscillating or steady flux and a strong acoustic excitation were also investigated. In this context, it was observed that the differences in the power spectra of the displacements in the steady and oscillating flux cases were primarily in the low frequency regime typical of the oscillating flux and were most significant when analyzing the inplane motions as compared to their transverse counterparts.

The last part of the present investigation focused on the development and first validation of an extended structural reduced order modeling approach in which the linear variations with local temperature of the structural properties, i.e. elasticity tensor and coefficient of thermal expansion, are accounted for. The form of the corresponding combined thermal-structural ROM was first determined. Next, an indirect strategy was developed for the evaluation of the unknown coefficients of the model from nonlinear static finite element computations. Finally, a simple validation example was treated for which an excellent matching of reduced order model and full Nastran predictions was observed.

REFERENCES

1. McEwan, M.I., Wright, J.R., Cooper, J.E., and Leung, A.Y.T. 2001. "A combined Modal/Finite Element Analysis Technique for the Dynamic Response of a Nonlinear Beam to Harmonic Excitation," *Journal of Sound and Vibration*, Vol. 243: 601-624.

2. Hollkamp, J.J., Gordon, R.W., and Spottswood, S.M. 2005. "Nonlinear Modal Models for Sonic Fatigue Response Prediction: A Comparison of Methods," *Journal of Sound and Vibration*, Vol. 284: 1145-1163.

3. Mignolet, M.P., Radu, A.G., and Gao, X. 2003. "Validation of Reduced Order Modeling for the Prediction of the Response and Fatigue Life of Panels Subjected to Thermo-Acoustic Effects," *Proceedings of the 8th International Conference on Recent Advances in Structural Dynamics*, Southampton, United Kingdom, Jul. 14-16.

4. Radu, A., Yang, B., Kim, K., and Mignolet, M.P. 2004. "Prediction of the Dynamic Response and Fatigue Life of Panels Subjected to Thermo-Acoustic Loading," *Proceedings of the 45th Structures, Structural Dynamics, and Materials Conference*, Palm Springs, California, Apr. 19-22. AIAA Paper AIAA-2004-1557.

5. Hollkamp, J.J., and Gordon, R.W. 2008. "Reduced-Order Models for Nonlinear Response Prediction: Implicit Condensation and Expansion," *Journal of Sound and Vibration*, Vol. 318: 1139–1153.

6. Przekop, A., and Rizzi, S.A. 2006. "A Reduced Order Method for Predicting High Cycle Fatigue of Nonlinear Structures," *Computers and Structures*, Vol. 84 (24-25): 1606-1618.

7. Kim, K., Wang, X.Q., and Mignolet, M.P. 2008. "Nonlinear Reduced Order Modeling of Functionally Graded Plates," *Proceedings of the 49th Structures, Structural Dynamics, and Materials Conference*, Schaumburg, Illinois, Apr. 7-10. AIAA Paper AIAA-2008-1873.

8. Kim, K., Khanna, V., Wang, X.Q., and Mignolet, M.P. 2009. "Nonlinear Reduced Order Modeling of Flat Cantilevered Structures," *Proceedings of the 50th Structures, Structural Dynamics, and Materials Conference*, Palm Springs, California, May 4-7. AIAA Paper AIAA-2009-2492.

9. Przekop A., and Rizzi S.A. 2006. "Nonlinear Reduced Order Random Response Analysis of Structures with Shallow Curvature," *AIAA Journal,* Vol. 44 (8): 1767-1778.

10. Gordon R.W., and Hollkamp, J.J. 2006. "Reduced-Order Modeling of the Random Response of Curved Beams using Implicit Condensation," *Proceedings*

of the 49th Structures, Structural Dynamics, and Materials Conference, Newport, Rhode Island, May 1-4. AIAA Paper AIAA-2006-1926.

11. Spottswood, S.M., Hollkamp, J.J., and Eason, T.G. 2008. "On the Use of Reduced-Order Models for a Shallow Curved Beam Under Combined Loading," *Proceedings of the 49th Structures, Structural Dynamics, and Materials Conference*, Schaumburg, Illinois, Apr. 7-10. AIAA Paper AIAA-2008-1873.

12. Przekop, A., and Rizzi, S.A. 2007. "Dynamic Snap-Through of Thin-Walled Structures by a Reduced-Order Method," *AIAA Journal*, Vol. 45 (10): 2510–2519.

13. Spottswood, S.M., Eason, T.G., Wang, X.Q., and Mignolet, M.P. 2009. "Nonlinear Reduced Order Modeling of Curved Beams: A Comparison of Methods," *Proceedings of the 50th Structures, Structural Dynamics, and Materials Conference*, Palm Springs, California, May 4-7. AIAA Paper AIAA-2009-2433.

14. Kim, K., Kim, Y.C., Mignolet, M.P., Liu, D.D., Chen, P.C., Lee, D.H. 2007. "Random Aeroelastic Response Due to Strong Hypersonic Unsteady-Wave/Shock Interaction with Acoustic Loads," *Proceedings of the 48th Structures, Structural Dynamics, and Materials Conference*, Honolulu, Hawaii, Apr. 23-26. AIAA Paper AIAA-2007-2014.

15. Liu, D.D., Wang, Z., Yang, S., Cai, C., Wang, X.Q., and Mignolet, M.P. 2009. "Nonlinear Aeroelastic Methodology for A Membrane-on-Ballute Model with Hypersonic Bow Shock," *Proceedings of the 50th Structures, Structural Dynamics, and Materials Conference*, Palm Springs, California, May 4-7. AIAA Paper AIAA-2009-2363.

16. Perez, R., Wang, X.Q., and Mignolet, M.P. 2011. "Nonlinear Reduced Order Models for Thermoelastodynamic Response of Isotropic and FGM Panels," *AIAA Journal*, Vol. 49 (3): 630-641.

17. Perez, R., Wang, X.Q., and Mignolet, M.P. 2010. "Steady and Unsteady Nonlinear Thermoelastodynamic Response of Panels by Reduced Order Models," *Proceedings of the 51st Structures, Structural Dynamics, and Materials Conference*, Orlando, Florida, Apr. 12-15. Paper AIAA-2010-2724.

18. Blevins, R.D., Holehouse, I., and Wentz, K.R. 1993. "Thermoacoustic Loads and Fatigue of Hypersonic Vehicle Skin Panels," *Journal of Aircraft*, Vol. 30: 971-978.

19. Fung, Y.C., and Tong, P. 2001. *Classical and Computational Solid Mechanics*. River Edge: World Scientific.

20. Bonet, J., and Wood, R.D. 1997. *Nonlinear Continuum Mechanics for Finite Element Analysis.* Cambridge: Cambridge University Press.

21. Vujosevic, L., and Lubarda, V. A. 2002. "Finite-Strain Thermoelasticity based on Multiplicative Decomposition of Deformation Gradient," *Theoretical and Applied Mechanics*, Vol. 28-29: 379-399.

22. Muravyov, A.A., and Rizzi, S.A. 2003. "Determination of Nonlinear Stiffness with Application to Random Vibration of Geometrically Nonlinear Structures," *Computers and Structures*, Vol. 81 (15): 1513-1523.

23. Nayfeh, A.H., and Mook, D.T. 1995. *Nonlinear Oscillations*. New York: Wiley.